Sub-optimal Lunar Landing GNC using Non-gimbaled Bio-inspired Optic Flow Sensors

Guillaume Sabiron, Thibaut Raharijaona, Laurent Burlion, Erwan Kervendal, Eric Bornschlegl, Franck Ruffier

▶ **To cite this version:**

Guillaume Sabiron, Thibaut Raharijaona, Laurent Burlion, Erwan Kervendal, Eric Bornschlegl, et al.. Sub-optimal Lunar Landing GNC using Non-gimbaled Bio-inspired Optic Flow Sensors. IEEE Transactions on Aerospace and Electronic Systems, 2015, IEEE TRANSACTIONS ON AEROSPACE AND ELECTRONIC SYSTEMS, 51 (4), pp.2525 - 2545. 10.1109/TAES.2015.130573 . hal-01270504

HAL Id: hal-01270504
https://hal.science/hal-01270504

Submitted on 8 Feb 2016

HAL is a multi-disciplinary open access archive for the deposit and dissemination of scientific research documents, whether they are published or not. The documents may come from teaching and research institutions in France or abroad, or from public or private research centers.

L'archive ouverte pluridisciplinaire **HAL**, est destinée au dépôt et à la diffusion de documents scientifiques de niveau recherche, publiés ou non, émanant des établissements d'enseignement et de recherche français ou étrangers, des laboratoires publics ou privés.

Sub-optimal Lunar Landing GNC using Non-gimbaled Bio-inspired Optic Flow Sensors

Guillaume Sabiron, Thibaut Raharijaona, Laurent Burlion, Erwan Kervendal, Eric Bornschlegl, and Franck Ruffier,

***Abstract*—Autonomous planetary landing is a critical phase in every exploratory space mission. Autopilots have to be safe, reliable, energy-saving, and as light as possible. The 2-D Guidance Navigation and Control (GNC) strategy presented here makes use of biologically inspired landing processes. Based solely on the relative visual motion known as the Optic Flow (OF) assessed with minimalistic 6-pixel 1-D OF sensors and Inertial Measurement Unit measurements, an optimal reference trajectory in terms of the mass was defined for the approach phase. Linear and nonlinear control laws were then implemented in order to track the optimal trajectory. To deal with the demanding weight constraints, a new method of OF estimation was applied, based on a non-gimbaled OF sensor configuration and a linear least squares algorithm. The promising results obtained with Software-In-the-Loop simulations showed that the present full GNC solution combined with our OF bio-inspired sensors is compatible with soft, fuel-efficient lunar spacecraft landing and might also be used as a backup solution in case of conventional sensor failure.**

LIST OF ABBREVIATIONS

GNC:	Guidance Navigation and Control
HG:	High Gate
LG:	Low Gate
LMS:	Local Motion Sensor
LROC:	Lunar Reconnaissance Orbiter Camera
MPC:	Model Predictive Control
OF:	Optic Flow
PANGU:	Planet and Asteroid Natural scene Generation Utility
SIL:	Software-In-the-Loop
TTC:	Time-To-Contact
VLSI:	Very Large Scale Integration
VMS:	Visual Motion Sensor

I. INTRODUCTION

The latest vision-based systems are of great interest for Guidance Navigation and Control (GNC) applications and are therefore being widely used in space exploration missions, especially during the entry, descent and landing phases. Several recent studies have focused on visual methods for estimating the position and velocity of spacecraft such as planetary landers [1]–[4] or performing hazard avoidance [5]. Most of these methods involve the use of cameras and other classical remote sensors such as RADAR (RAdio Detection And Ranging) or LIDAR (LIght Detection And Ranging) devices [6]. To deal with potential failure of the main sensors, the latest small spacecraft often feature redundant conventional sensors that are heavy, bulky and highly energy-consuming. In the case of a backup solution, our strategy presented here, featuring lightweight sensors do away with redundant heavy equipment of this kind.

The need for miniature GNC devices entails challenging constraints in terms of weight, size, cost, and power consumption. Developing advanced miniature GNC sensors is an important challenge for the years to come: these requirements could possibly be met, for instance, by combining the advantages of visual sensors, LIDAR, and RADAR in a small, lightweight, low-cost GNC sensor. In parallel with the time-consuming size-reduction efforts involved in reaching these goals, it is necessary to develop an efficient, reliable sensor fusion algorithm to compensate for the losses incurred by the miniaturization. Another alternative might be to apply an innovative robotic approach to lunar landing problems: miniature biologically-inspired sensors could be developed, for example, based on the visual cues used by tiny airborne creatures such as insects to control their flight.

Based on their previous neurophysiological studies on the fly's eye, Franceschini et al. [7] developed a simple principle, which was subsequently called the "Time of Travel principle" (see Fig. 3). This algorithm can be used to calculate the angular velocity of the images sweeping backward across the view field in one direction forming the 1-D Optic Flow (OF), which is detected by a small device known as a 2-pixel Local Motion Sensor (LMS) (see [8]–[10] for several implementations). Nature has shown the great potential of the rich visual OF information used by flying insects [7], [11], [12] to perform hazardous robotic tasks in complex, unknown environments. OF processing methods could be used in control systems in several ways:

- First as a means of estimating the usual states of the system in combination with other more classical sensors such as Inertial Measurement Units (IMUs), sonars, GPS, and/or accelerometers [13],
- Secondly, OF data can be used directly in a control loop without any need for information about the velocity, acceleration, altitude or even about the characteristics of the terrain, and hence without any bulky, power-consuming sensors. Many OF based robotic control systems have been developed which are able to perform take-

G. Sabiron, T. Raharijaona and F. Ruffier are with Aix-Marseille University, CNRS, ISM UMR7287, Biorobotics Department, 13288, Marseille cedex 09, France (e-mail: Thibaut.Raharijaona@univ-amu.fr; Franck.Ruffier@univ-amu.fr).

G. Sabiron and L. Burlion are with ONERA - French Aerospace Lab (ONERA, Systems Control and Flight Dynamics -DCSD-), Toulouse 31055, France (e-mail: Guillaume.Sabiron@ifpen.fr; Laurent.Burlion@onera.fr).

E. Kervendal is with Airbus Defence and Space, Toulouse, France (e-mail: Erwan.Kervendal@astrium.eads.net).

E. Bornschlegl was with the European Space Agency (ESTEC), 2200 AG Noordwijk, The Netherlands.

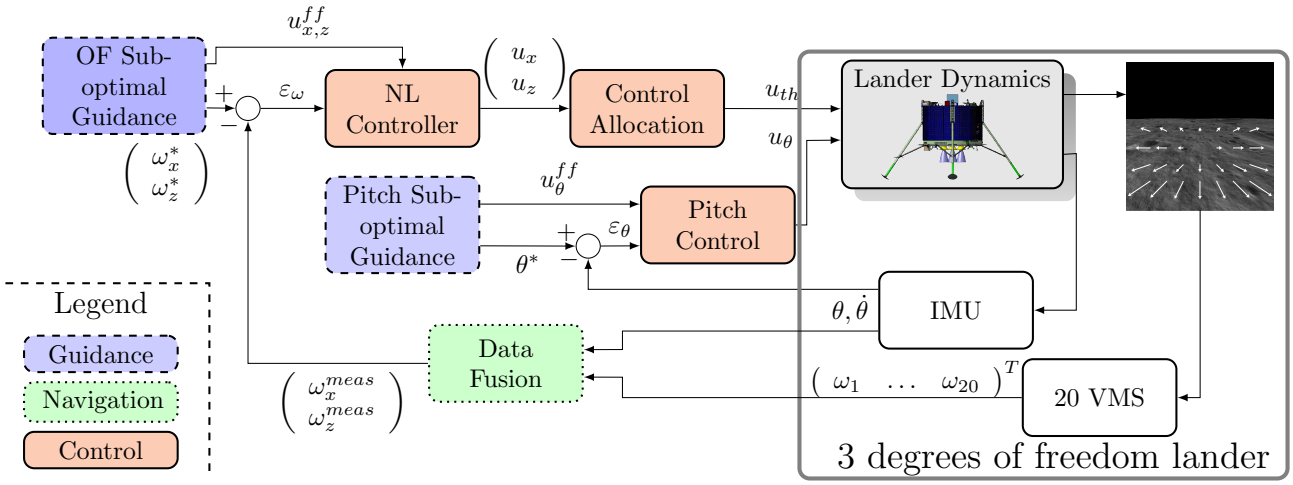

Fig. 1. Sketch of the full GNC solution presented in this paper. In the non-gimbaled sensor configuration presented here, twenty 6-pixel VMSs feed the data fusion block along with an IMU. The data fusion block based on a linear least squares algorithm feeds the nonlinear controller with the high interest OF values estimated. The control allocation block transforms the control signal into a braking force defining the magnitude of the thrust vector. The inner attitude control loop delivers the control signal u_θ assessed via a linear output feedback controller and the sub-optimal guidance strategy defining the orientation of the thrust vector. The reference signals $\omega_x^*(t)$, $\omega_z^*(t)$ and $\theta^*(t)$ are precomputed using nonlinear programming methods.

off, terrain-following and landing safely and efficiently by mimicking insects' behavior [9], [14], avoiding frontal obstacles [15]–[18], tracking a moving target [19] as well as hovering and landing on a moving platform [20],

- Finally, the OF has been used to extract relative-state information for navigation purposes in the Wide Field Integration methods presented by [21]–[23].

Several spacecraft landing studies have been recently performed by using direct means of regulating the downward OF (measured in the local vertical direction) and the Time To Contact (TTC, an index to the ground height, i.e., the local altitude, divided by the vertical velocity) to achieve soft landing. In [24], the authors presented the first simulations involving neuromorphic principles to process the 1-D OF and make a successful autonomous lunar landing. The autopilot used only the OF and the acceleration to regulate the spacecraft's flight without any need for velocity and height estimates or measurements. Results obtained in [24], [25] in terms of final velocities, pitch, and power consumption were too large to be compatible with the soft and fuel-efficient landing requirements: nevertheless, the autopilot's performances were assessed by running simulations on PANGU software (Planet and Asteroid Natural scene Generation Utility) developed for ESA by the University of Dundee (see [26], [27] for further information). PANGU is a tool which can be used to simulate visual environments on planetary surfaces. In 2011, Izzo et al. [28], [29] calculated optimal trajectories in terms of the duration of the landing phase and the fuel consumption by performing numerical simulations: the authors compared the fuel consumption penalty involved in various ventral OF and TTC-based flight paths imposed in open loop. Lastly, in [30], [31], optimal control and image processing were combined in a nonlinear Model Predictive Control (MPC) coupled to a state estimation scheme based on a sensor fusion process; with this MPC control strategy, the optimal control sequences had to be computed online at each time step.

In all these previous studies [24], [25], [28]–[31], the OF sensors were assumed to be always pointing vertically downward, which required the use of additional gimbal actuated systems that are too bulky for small planetary landers. Here, sub-optimal soft lunar landing performances were achieved using bio-inspired principles and devices without any state estimation methods, bulky classical sensor suites (such as RADAR, LIDAR, cameras, etc.), and especially, without any gimbal systems.

Step by step, the full GNC solution featuring several OF sensors fixed to the lander's structure, two control loops acting in parallel to make the spacecraft follow a pre-calculated mass optimal OF-based trajectory and requiring few online computational resources was developed. The reference OF profiles were neither constant nor did they take the form of classical functions: they were computed to avoid unnecessary fuel expenditure thanks to the use of optimal control tools. The reference trajectory computed (including the OF profiles) is optimal in terms of the fuel consumption during the nominal descent trajectory. The guidance scheme is said to be sub-optimal since it provides the control laws with the offline-computed trajectory, which might not be completely optimal during the actual descent due to the occurrence of tracking errors. A linear least squares algorithm was used here to estimate high interest OF values using several sensors oriented in different directions fixed to the structure. A dedicated method of determining the appropriate number of OF sensors was applied. To the best of our knowledge, no previous studies have addressed the problem of non-gimbaled OF sensors in the planetary landing context. Special efforts were made here with the simulations in order to develop a Matlab/Simulink simulator which was as realistic as possible. The OF sensor model used in the present Software-In-the-Loop (SIL) simulations with the PANGU environment benefited from recent

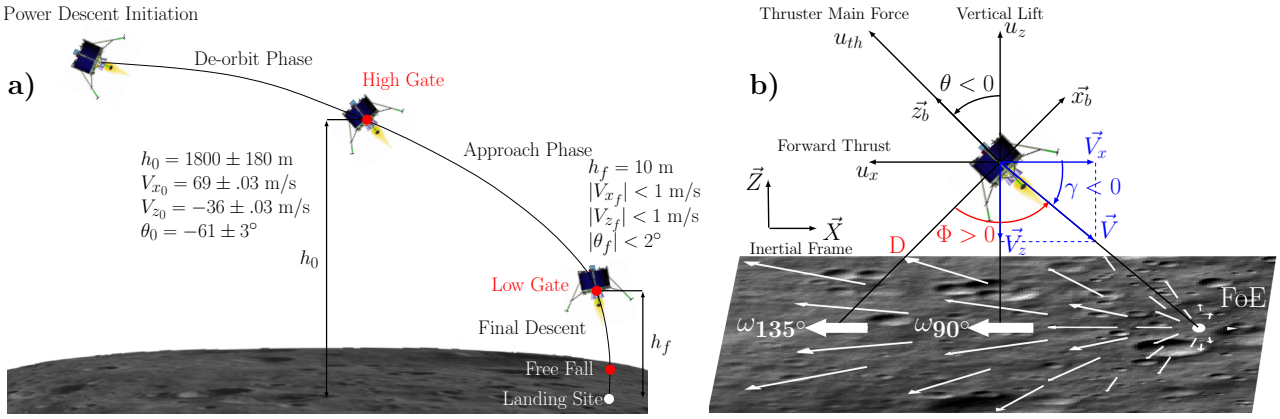

Fig. 2. Reference trajectory for lunar landing and notations (Lander sketch: by courtesy of Airbus Defence and Space (previously named ASTRIUM EADS). a) The landing phase addressed in this study is defined as that between High Gate (HG) and Low Gate (LG) and called the approach phase. The objectives of the lander are to reach LG (at a height of 10 m) at both vertical and horizontal velocities of less than 1 m/s (in absolute values) and a pitch angle in the $\pm 2°$ range. Modified from [32]. b) Diagram of the lander in a planar motion, showing the inertial reference frame ($\vec{X}$, $\vec{Z}$), the velocity vector $\vec{V}$, the mean thruster force u_{th}, and its projections in the Local Vertical (collinear to $\vec{Z}$ axis) Local Horizontal (collinear to $\vec{X}$ axis) (LVLH) reference frame. Two specific optic flows are depicted on the lunar surface $\omega_{90°}$ and $\omega_{135°}$. It can be noted that the point in the direction of motion of the lander is called the focus of expansion (FoE) and has an OF equal to zero. Adapted from [33].

advances in 6-pixel Visual Motion Sensors (VMS) [34], which are self-contained devices. These VMSs involving analog and digital filtering stages as well as a contrast thresholding step were previously installed onboard a real large scale Unmanned Aerial Vehicle [35].

In Section II, the method used to design the full GNC solution and the landing scenario is presented. In Sections III and IV, the high-interest OF measurement variables, nonlinear dynamic model and vision-based SIL simulations are defined. In Section V, we describe how sub-optimal guidance laws were computed by performing nonlinear programming. Section VI describes the nonlinear controller based on Lyapunov theory developed for the OF feedback loop and the linear controller developed for the pitch feedback loop. In Section VII, we discuss the challenge involved in using non-gimbaled sensors and present a method based on a least squares algorithm. The full-GNC results were obtained by performing SIL simulations to calculate the fuel consumption and the final velocities (see Section VIII). Lastly, Section IX describes some paths for future research and ends with some final comments.

II. Scenario definition and its full GNC solution

In this paper, we present the full GNC solution for lunar landing step by step (see Fig. 1) by:

- describing the dynamic model for the lander,
- defining the sub-optimal guidance laws with respect to the lander's fuel-consumption in terms of the OF and the pitch trajectories,
- developing a nonlinear controller based on Lyapunov theory,
- suggesting a control allocation scheme,
- fusing the 20 local OF measurements into relevant OF measurements for trajectory tracking,
- simulating the full GNC solution using a lunar environment simulated with PANGU software.

The lunar landing trajectory was divided into the following four phases (see Fig. 2.a):

1) De-orbit Phase,
2) Approach Phase,
3) Final Descent,
4) Free Fall.

The approach phase from High Gate (HG) (1800 m $\pm 10\%$ Above Ground Level -AGL-) to Low Gate (LG) (10 m AGL) defines the autonomous lunar landing problem. HG corresponds to the height at which the landing site can be detected by the spacecraft's visual system. LG corresponds to the height at which visual contact with the landing site is no longer possible due to the lunar dust raised by the thrusters. When reaching the LG, another GNC strategy is expected to take control of the final descent. Initial parameters are the horizontal velocity ($V_{x_0} = 69 \pm .03$ m/s), vertical velocity ($V_{z_0} = -36 \pm .03$ m/s), pitch angle ($\theta_0 = -61 \pm 3°$), ground height ($h_0 = 1800 \pm 180$ m), and lander's mass ($m_{ldr_0} = 762 \pm 11$ kg) (see Fig. 2.a).

This reference trajectory is therefore very similar to that involved in the Apollo test case scenario often used in the literature [36]. The solution targeted involves the following demanding final constraints at LG ($h_f = 10$ m):

- $|V_{x_f}| \leq 1$ m/s,
- $|V_{z_f}| \leq 1$ m/s,
- $|\theta_f| < 2°$.

The objectives are thus defined in terms of the velocity and the attitude. The position on the x-axis is not dealt with here since we are aiming at soft landing without any requirements about the final downrange. With the present approach, the propellant consumption will be decreased as far as possible by the autonomous lunar landing strategy. The main difficulty to be overcome is that the entire state vector is not given by the measurements. For instance, the velocities and positions are neither measured nor estimated: only the angular rates,

attitude, mass, and OF are measured and thus available for use as inputs to the controllers. To achieve soft lunar landing, the autopilot must be able to reduce the magnitude of its velocity vector and control the orientation of the velocity vector, which is called the flight path angle and denoted γ (see Fig. 2.b). This was achieved by jointly adjusting the lander's two available control signals: its pitch and its main thrust.

In this study, the approach phase is first defined by determining an optimal fuel-saving trajectory by computing the control sequence that requires the least fuel to reach the LG and complies with the demanding final constraints. The second step corresponds to following this trajectory during the actual landing phase, using IMU measurements, OF measurements, and linear/nonlinear controllers.

The GNC strategy described above is designed to take over control at the high gate. However, regarding backup solution application, if a sensor failure occurs, the GNC solution might suffice to control the system. Indeed in the case of a backup solution, the sensor failure might happen at any time between the high gate and the low gate. In this configuration, to initialize the GNC architecture, the last known value of the states (height, velocity, and attitude) could be used to switch to the corresponding part of the reference trajectory.

III. Lunar Lander Dynamic Model and Optic Flow Equations

The autopilot consists here of an OF-based control system operating in the vertical plane $(\vec{X}, \vec{Z})$, which controls the spacecraft's main thruster force and pitch angle. To stabilize the lander, it is necessary to cope with nonlinearities and the inherent instability of the system. Since the lunar atmosphere is very thin, no friction or wind forces are applied to the lander. In the present model, the heave and surge dynamics are coupled via the lander's pitch (see Fig. 2.b). To incorporate the physical constraints into the model in line with the ESA/Airbus Defence and Space preliminary studies, the following assumptions are adopted:

$$(\textbf{\textit{H1}}) \quad \begin{cases} \textit{The braking thrusters can produce only positive forces and the} \\ \textit{thrust is limited to 3820 N, which means } 0 \leq u_{th} \leq \textit{3820 N}. \end{cases}$$

$$(\textbf{\textit{H2}}) \quad \begin{cases} \textit{The attitude thrusters can produce forces up to} \\ 44 \textit{ N, which means } -44 \leq u_\theta \leq 44 \textit{ N}. \end{cases}$$

In line with the ESA/Airbus Defence and Space preliminary studies, few other values related to thrusters performances, lander's characteristics and physical constants are defined in table I.

TABLE I
Constant parameters based on ESA/Airbus Defence and Space studies

Specific impulse (s)	Gravitational acc. (m/s^2)	Initial mass (kg)
$I_{sp_{th}} = 325$	$g_{Earth} = 9.81$	$m_{ldr}(t_0) = 762$
$I_{sp_\theta} = 287$	$g_{Moon} = 1.63$	

The specific impulse I_{sp}, an efficiency parameter defined by the ratio between the thrust and the mass flow rate times the Earth's gravitational acceleration constant $(I_{sp_{th}} = u_{th}/(\dot{m}_{ldr}.g_{Earth}))$ is denoted $I_{sp_{th}}$ in the case of the braking thrusters and I_{sp_θ} in that of the attitude thrusters. The lunar acceleration due to the gravity is taken to be constant due to the low initial altitude

In line with previous authors' assumptions, the lunar ground is taken to be flat (with an infinite radius of curvature) [37]. The dynamic motion of the lander can be described in the time domain by the following dynamic system in the inertial frame $\mathcal{I}$ associated with the vector basis $(\vec{X}, \vec{Z})$:

$$\begin{cases} a_{ldr_z}(t) = \dfrac{\cos(\theta(t))}{m_{ldr}(t)} u_{th}(t) - g_{Moon} \\ a_{ldr_x}(t) = \dfrac{\sin(\theta(t))}{m_{ldr}(t)} u_{th}(t) \end{cases} \tag{1}$$

where u_{th} corresponds to the control force applied to the lander, $a_{ldr_{x,z}}$ are the lander's accelerations in the lunar inertial reference frame, m_{ldr} stands for the lander's mass, θ is the pitch angle, t denotes the time, and g_{Moon} denotes the lunar acceleration due to the gravity. The pitch dynamics of the system are modeled as follows:

$$\frac{I}{R}\frac{d^2\theta}{dt^2} = u_\theta(t) \tag{2}$$

where u_θ is the input signal controlling the spacecraft's pitch and θ is assessed independently via an IMU, I is the moment of inertia, and R is the eccentricity of the attitude thrusters with respect to the center of mass. The lander's mass depends directly on the fuel consumption, as given by the following relation:

$$\dot{m}_{ldr}(t) = \frac{-u_{th}(t)}{I_{sp_{th}}.g_{Earth}} + \frac{-|u_\theta(t)|}{I_{sp_\theta}.g_{Earth}} \tag{3}$$

This means that:

$$m_{ldr}(t) = m_{ldr}(t_0) - \frac{1}{g_{Earth}} \int_{t_0}^{t} \left(\frac{u_{th}(\epsilon)}{I_{sp_{th}}} + \frac{|u_\theta(\epsilon)|}{I_{sp_\theta}} \right) d\epsilon \tag{4}$$

Since the initial mass is known and the lander's mass depends linearly on the integral of the lander's thruster control signal, the mass can be computed and assessed at any time during the descent.

Once the dynamic model of the spacecraft has been defined, one needs to state the OF equations to find what information can be deduced from this visual cue. The general OF $\omega(\Phi)$ can be described as the sum of the two distinct components defined by [38], e.g. the translational and rotational OF in the vertical plane as follows:

$$\omega(\Phi) = \omega_T + \omega_R \tag{5}$$

The translational OF ω_T depends on the linear velocity V expressed in the inertial frame, the distance from the ground D in the gaze direction and the elevation angle Φ (i.e. the angle between the gaze direction and the heading direction).

$$\omega_T = \frac{V}{D}\sin(\Phi) \tag{6}$$

See Fig. 2.b for geometric notations.

The rotational OF ω_R depends only on the angular velocity Ω_j expressed in the body's fixed frame $\mathcal{B}$ associated with the vector basis $(\vec{x_b}, \vec{z_b})$, where j denotes the axis of rotation, and

on the elevation angle, λ, between the gaze direction and the axis of rotation.

$$\omega_R = \Omega_j \sin(\lambda) \tag{7}$$

On the vertical plane, $\lambda = \frac{-\pi}{2}$ and $\Omega_j = \dot{\theta}$ and hence, $\omega_R = -\dot{\theta}$. Lastly, on the 2-D plane, the ground-truth OF can be monitored as follows:

$$\omega_{grd-trh} = \frac{V}{D}\sin(\Phi) - \dot{\theta} \tag{8}$$

For the sake of clarity, the specific local translational optic flow $\omega_T(\Phi)$ will be written as follows:

- ω_{90° in the case of the downward OF, i.e. in the nadir direction (90° between the gaze direction and the local horizontal)
- and, ω_{135° in that of the OF oriented at 135° from the local horizontal.

An illustration of ω_{90° and ω_{135° is presented in Fig. 2.b. From the previous equation, from the point of view of hazardous obstacle avoidance, it can be seen that whenever an obstacle appears in the OF sensor's line of sight, the distance D to the obstacle will be decreased or increased depending on whether it is a boulder or a crater: it will cause the autopilot to react by decelerating or accelerating accordingly so as to ensure the lander's soft descent regardless of the topology of the terrain. The rotational OF ω_R is subtracted from the general OF $\omega(\Phi)$ (see (5)), using the lander's mechanical rotation sensed by the IMU in order to benefit from the useful properties of the translational OF ω_T: this operation is known as the derotation process [39].

Taking equation (6), under the assumption that the ground is practically flat (i.e. $D = h/\cos(\frac{\pi}{2} - \Phi + \gamma)$, where γ denotes the flight path angle (the orientation of the velocity vector with respect to the local horizontal as described in Fig. 2.b) and $\Phi - \gamma$ denotes the angle between the gaze direction and the local horizontal), then:

$$\omega_{90^\circ} = \frac{V_x}{h} \tag{9}$$

with $V = V_x/\cos(\gamma)$ and h the ground height.

For $\Phi - \gamma = 135^\circ$:

$$\omega_{135^\circ} = \frac{V}{2h}(\cos(\gamma) - \sin(\gamma)) = \frac{\omega_{90^\circ}}{2}(1 - \tan(\gamma)) \tag{10}$$

where $\tan(\gamma) = \frac{V_z}{V_x}$.

Lastly, the relevant values of OF, i.e., the ventral OF ω_x and the expansion OF ω_z used in the present regulators are then expressed directly in terms of ω_{90° and ω_{135°:

$$\omega_x = \frac{V_x}{h} = \omega_{90^\circ} \tag{11}$$

$$\omega_z = \frac{V_z}{h} = \omega_{90^\circ} - 2\omega_{135^\circ} \tag{12}$$

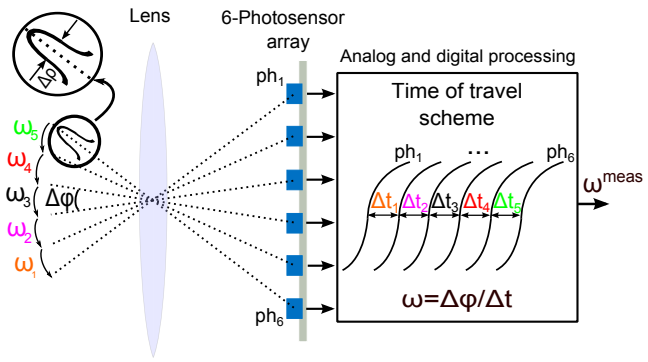

Fig. 3. Simplified processing algorithm of the VMS. Adapted from [34].

IV. Simulated Visual Environment: PANGU Software and Optic Flow Sensor Model

To enhance the realism of the simulation, PANGU software was used to generate images of the lunar surface, taking the position of the system, the elevation of the sun and the camera's properties into account. The simulated lunar surface was irregular and sometimes included craters up to 40 m deep. The images generated by PANGU contained 256 gray-scale levels and had a resolution of 256×256 pixels.

Each OF sensor included six photoreceptors: the visual axes of each pair of photoreceptors were separated by the inter-receptor angle $\Delta\varphi = 0.1^\circ$. The angular sensitivity of each photoreceptor obeyed a 2-D Gaussian function mimicking the angular sensitivity of the fly's photoreceptor with the acceptance angle (the angular width at half height) $\Delta\rho = \Delta\varphi = 0.1^\circ$. A simplified model of the processing algorithm of the VMS is presented in Fig. 3. Five OF are computed for each pair of photodiodes but only the median value is delivered as an output at 2kHz (a full description of the algorithm can be found in [35]). As soon as a contrast is detected, the time of travel algorithm calculates the time Δt elapsing between its detection by two adjacent photodiodes. The OF is directly computed using this equation $\omega = \Delta\varphi/\Delta t$. These small inter-receptor and acceptance angle values make it possible to compute very low velocities. Since we have such a narrow field of view, even high spatial frequency contrasts will be detected by the photodiodes, which is very helpful at low OF levels, where fewer contrasts occur in the sensor's line of sight.

In the simulated VMS model, the photoreceptors' output is simulated at each simulated time step (1 ms) by convolving the PANGU-generated lunar surface image with the 2-D Gaussian filter. The simulated 6-pixel VMSs then assess the OF. The Matlab/Simulink model of the 6-pixel VMS is exactly the same as that embedded in the real OF thus providing SIL[1].

To validate the simulated sensor model in a realistic visual environment, we implemented, simulated and analyzed the above improvements on Lunar Reconnaissance Orbiter Camera (LROC) images[2]. We also compared the sensor output obtained in a LROC simulation with the results obtained

[1]Toolbox used for rapid prototyping available at http://www.kerhuel.eu
[2]Images available at http://lroc.sese.asu.edu

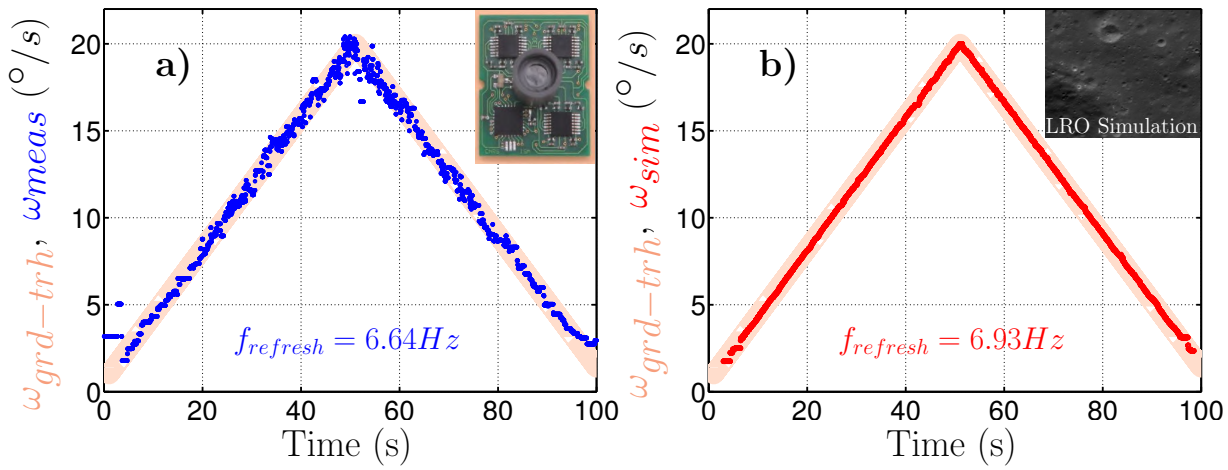

Fig. 4. Comparison between the real dynamic response of the low speed 6-pixel VMS (a - Modified from [35]) and the output of the simulated VMS on a LROC image (b). Rotations from 1°/s to 20°/s were applied to the sensor, which was designed to operate in the 1.5°/s to 25°/s range.

outdoors with a real-life implementation of the low speed 6-pixel VMS, upon applying the same angular speed pattern.

As shown in Fig. 4, the characteristics of the sensor model were found to be very similar to those of the real-life implementation of the 6-pixel VMS. The OF measured closely matched the reference signal, with a refresh rate of 6.64Hz in the case of the real measurements and 6.93Hz in that of the simulated VMS to which LROC images were applied. Since the visual environment differed between the simulation (lunar ground) and the real-life experiment (scrubland on a sunny day), the simulated results were expected to be more satisfactory. It is worth noting that the simulated sensor responded appropriately to a LROC image by following precisely the OF reference signal called $\omega_{grd-trh}$ without any outliers. Likewise, the results obtained in the outdoor experiments with an actual 6-pixel VMS were also accurate. The OF sensor code therefore proved to be fairly reliable when working with PANGU.

Although interesting results were obtained with LROC images, the fixed resolution of 0.24 m/px decreased the realism of the simulation at low altitudes. We therefore decided to use PANGU instead, which gives images with a variable resolution depending on the lander's height and attitude. PANGU yielded images with a definition of 256×256 px, regardless of the lander's position and attitude, which is nearer to reality. The main drawback of simulations involving the use of PANGU is the duration of the landing simulation. The approach phase lasts around 50 seconds, which means making 50000 TCP-IP requests to PANGU from Matlab/Simulink plus the remaining calculations required by the closed-loop system. A simulation involving two 6-pixel VMSs took 4.5 hours on an Intel® Core i7-2600 @ 3.40GHz and another one with twenty 6-pixel VMSs took more than 26 hours. This explains why the results of only two of these time-consuming closed-loop simulations are presented in this paper.

V. Offline Computation of the Optimal Fuel-Efficient Optic Flow Reference Trajectory

We need to find an OF-based trajectory to be followed during landing. A valid strategy previously studied in literature was that obtained by keeping the OF constant around the value defined by the final constraints. For instance, the first possibility would be to set the reference value at $\omega_{x_{ref}} = \frac{V_{x_f}}{h_f} = 0.1$rad/s in order to reach 10m at a velocity equal to or lower than 1m/s. However, at the beginning of the trajectory, the OF is lower than this reference value during a few seconds ($\frac{V_{x_0}}{h_0} \approx 0.04 < 0.1$ rad/s with $V_{x_0} = 69$m/s and $h_0 = 1800$m). This would cause the lander to accelerate horizontally and/or vertically in order to reach the reference value: it would instantaneously decrease its height and thus increase the OF. However, there is no need to reach 0.1rad/s so quickly or to wait without applying any actuation until the OF increases spontaneously, because the main goal here is to gradually brake the system efficiently while meeting the final constraints in terms of the overall fuel consumption.

Based on these findings, we decided to compute and analyze the optimal trajectory in order to obtain OF reference signals corresponding to the least fuel-consuming trajectory. The mass optimization problem was defined here along with the associated constraints, and its solution was computed in terms of the trajectory and the OF profiles.

In order to meet the low computational requirements, the optimal problem was solved offline only once: the OF and pitch profiles were determined and implemented in the form of constant vectors in the lander.

First of all, the optimal control sequence $u^* = \left(u^*_{th}, \ u^*_\theta \right)$ was computed, taking u^*_{th} to denote the braking thrust and u^*_θ to denote the pitch force (the upper script * indicates the optimality in terms of the mass, i.e., the fuel consumption). In this paper, optimality refers to the outputs of the optimization problem $\left(u^*_{th}, \ u^*_\theta \right)$ and the associated reference trajectory $(V^*_x, \ V^*_z, \ h^*, \ \theta^*)$.

Looking for the least fuel-consuming trajectory is equivalent to finding the control sequence u^* that minimizes the use of

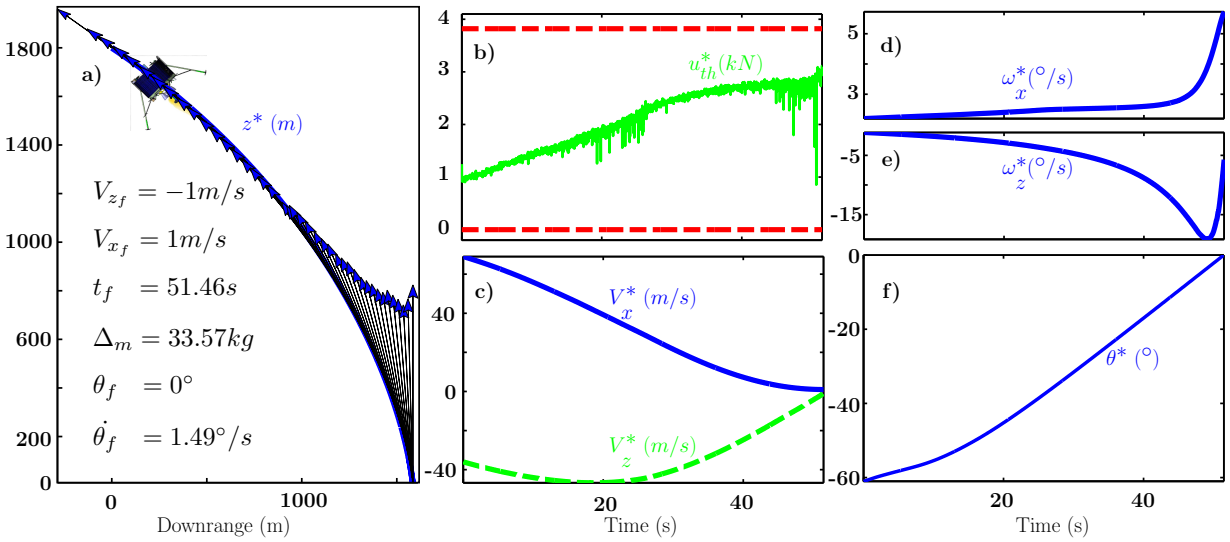

Fig. 5. Open loop trajectory under the optimal control sequences u^*_{th} and u^*_θ. a) Height h^* versus downrange x^*, orientation and normalized magnitude of the optimal control u^*_{th}. b) Optimal control sequence $u^*_{th} = \sqrt{u^{*2}_x + u^{*2}_z}$. The saturation imposed on the control signals u^*_{th} was chosen so that 0 N $\leq u^*_{th} \leq$ 3438 N. c) Velocities V^*_x, V^*_z. d-e) Optimal reference OF profile versus time. f) Pitch reference trajectory θ^* obtained under the optimal control sequence u^*_θ.

the control signal (see (3)).

The optimization problem can then be expressed as follows:

Solve

$$\min_{u_{th}(t),u_\theta(t)} \int_{t_0}^{t_f} \left(u_{th}(t) + |u_\theta(t)|\right)\, \mathrm{d}t \tag{13}$$

subject to

$$\begin{pmatrix} \dot{V}_z \\ \dot{V}_x \\ \dot{z} \\ \dot{x} \\ \ddot{\theta} \\ \dot{m} \end{pmatrix} = \begin{pmatrix} \frac{\cos(\theta)}{m} u_{th} - g_{Moon} \\ \frac{\sin(\theta)}{m} u_{th} \\ V_z \\ V_x \\ \frac{I}{R} u_\theta \\ \frac{-u_{th}}{I_{sp_{th}} \cdot g_{Earth}} + \frac{-|u_\theta|}{I_{sp_\theta} \cdot g_{Earth}} \end{pmatrix} \tag{14}$$

$$\begin{cases} V_z(t_0) = -36 \text{ m/s}, & \left|V_{z_f}\right| < 1 \text{ m/s} \\ V_x(t_0) = 69 \text{ m/s}, & \left|V_{x_f}\right| < 1 \text{ m/s} \\ h(t_0) = 1800 \text{ m}, & h_f = 10 \text{ m} \\ \theta(t_0) = -61°, & |\theta_f| < 2° \end{cases} \tag{15}$$

$$\begin{cases} 0 < u_{th} < 3438 \text{ N} \\ -44 < u_\theta < 44 \text{ N} \quad \forall t \in [t_0, t_f] \\ (-V_z, V_x, h, x) > 0 \\ \left|\dot{\theta}\right| < 1.5°/\text{s} \end{cases} \tag{16}$$

This offline optimal control problem was implemented using Matlab optimization software on the nonlinear system under constraints to bring the system from HG to LG. To solve this continuous time optimization problem, many freely available Matlab toolboxes using various methods can be used. The solution provided by ICLOCS (Imperial College London Optimal Control Software, [40]) based on the IPOPT solver suited our needs for the numerical implementation of a nonlinear optimization procedure in the case of the continuous system subjected to boundary and state constraints using the interior point method. The simulation of the open loop optimal control was therefore run on the nonlinear system to assess the optimal OF and pitch profiles $\left(\ \omega^*_x,\ \ \omega^*_z,\ \ \theta^*\ \right)$.

Equation (14) describes the dynamic lander model, (15) the initial and final conditions and (16) the actuator and system constraints along the trajectory. For safety reasons, a 10% clearance from the thrusters' physical saturation is added when pre-computing the optimal trajectory. This supplementary constraint gives the lander greater maneuverability around the pre-computed trajectory in closed loop. It is worth noting that a terminal constraint could be added if required to the downrange x to make pinpoint landing possible, but this might greatly increase the fuel consumption.

Since it may occur that $\dot{\theta} = -\omega_R > \omega_T$ and thus $\omega_{measured} < 0$, we had to use a two-directional version of the 6-pixel VMS adapted for use in the following measurement range: $\omega_{measured} \epsilon\, [-20°/\text{s};\ -0.1°/\text{s}] \cup [0.1°/\text{s};\ 20°/\text{s}]$ (see Sec. IV)

The fuel consumed decreases the lander's mass by Δm, which is defined as the difference between the initial and final mass of the lander $\Delta m = m_{ldr_0} - m_{ldr}(t_f)$ where $m_{ldr_0} =$ 762 kg and

$$m_{ldr}(t_f) = m_{ldr}(t_0) - \frac{1}{g_{Earth}} \int_{t_0}^{t_f} \left(\frac{u_{th}(\epsilon)}{I_{sp_{th}}} + \frac{|u_\theta(\epsilon)|}{I_{sp_\theta}} \right) d\epsilon \tag{17}$$

To ensure that the sum $\omega_{grd-trh} = \omega_T + \omega_R$ does not cancel itself out (i.e. $\omega_T = -\omega_R$), the pitch rate ($\omega_R = \dot{\theta}$) was constrained as follows: $\left|\dot{\theta}\right| = |\omega_R| < 1.5°/s$.

Under all these conditions, the optimal control sequences $(u^*_{th},\ u^*_\theta)$ were processed: the optimal solution was obtained with $t_f = 51.46$s and a decrease in the mass of $\Delta m < 33.6$ kg (amounting to 4.4% of the initial mass).

The trajectory computed under these constraints can be said to be optimal in the case of a more highly constrained problem than the system fully allows (due to the addition of constraints on $\dot{\theta}$ and the 10% margin on the thrust to account for the sensors' and actuators' operating ranges). In any case, both of these additional constraints (the pitch rate and the 10% margin added to the thrust) result in a very similar fuel expenditure to that obtained without them (amounting to a difference of only 0.21%).

Controlling the nonlinear system using the precomputed sequences $(u^*_{th},\ u^*_\theta)$ gives an idea of the optimal trajectory taken by the lander to reach the final conditions targeted. Figure 5 gives an overview of the evolution of the states and outputs during the landing phase when the nonlinear system is subjected to the optimal open-loop control sequences $(u^*_{th},\ u^*_\theta)$. Figure 5.a gives the trajectory of the lander in the plane and shows the evolution of the orientation and the normalized magnitude of the optimal control signal u^*_{th}. Figure 5.b presents the optimal control sequence $u^*_{th} = \sqrt{u^{*^2}_x + u^{*^2}_z}$. It can be seen from this figure that the control signal u^*_{th} delivered never reaches either the upper or the lower saturation, and that the variations are quite smooth during the entire trajectory. Figure 5.c shows the evolution of the vertical and horizontal velocities (in the LVLH frame), which meet the terminal constraints at t_f. The nonlinear control strategy described below in Sec. VI is used to perform the tracking of the optimal OF profiles presented in Fig. 5.d-e

It is worth mentioning that in the optimal control problem, the HG conditions are taken to be constant values. These nominal values are not necessarily reached when this GNC solution is switched on. As described in II, the initial height, velocity and mass can vary at HG. We decided to compute only one optimal trajectory from the initial HG conditions to the expected final conditions and let the nonlinear controller cancel any tracking errors which occur. An improvement to the guidance scheme could be made by solving the optimal control problem several times at various initial altitudes covering the admissible range. A bank of reference trajectories could be embedded into the GNC computer, and a selection algorithm would eventually choose the best suitable candidate trajectory at the actual HG on the basis of the available measurements. This enhanced guidance scheme would still be sub-optimal since the trajectories would be computed offline, but the initial errors with respect to the actual position and reference position would be greatly reduced.

As can be expected, neither the optimal OF profiles nor the ventral OF ω^*_x nor the expansion OF ω^*_z, are constant during the entire descent phase. The OF profiles end up as follows:

- ω_z decreases slowly down to $-19.16°$/s before increasing sharply toward $\omega_{z_f} = -5.7°$/s,
- ω_x increases linearly during the first half of the descent up to $2.5°$/s and then exponentially up to $\omega_{x_f} = 5.7°$/s.

The inner loop dynamics (i.e., the pitch evolution) are presented in Fig. 5.f under the optimal pitch control signal u^*_θ: the pitch starts at $-61°$ and ends up at $0°$, as was to be expected.

The final velocities are such that $V_{x_f} = -V_{x_f} = 1$m/s. In the final velocity ranges specified in 15, the solution is optimal in terms of the fuel expenditure (the task is less demanding in terms of braking). If tracking errors occur during the actual landing, this might prevent final objectives from being met. Another way of setting the constraints on the system's states would be to require that $V_{x_f} = -V_{x_f} = 0$m/s, thus increasing the error margin allowed at LG in the final velocities.

At this point, optimal, fuel-efficient, OF reference signals as well as pitch reference signal were computed along with the control sequences $(u^*_{th},\ u^*_\theta)$ using nonlinear programming methods.

VI. Control law design

A. Optic-flow nonlinear control

Once the optimal OF reference trajectory had been defined, we had to design the control laws required to close the loop based on the OF measurements obtained during the descent. Nonlinear controllers were therefore designed for this purpose, including a feedforward term based on the given optimal control sequences and output feedback with ω_x and ω_z measurements. Since both the height and the velocity show considerable variations during the approach phase, it was decided not to linearize the system around an equilibrium point, which would have differed from the actual dynamics most of the time. No state estimation methods, but only the visual OF cues $\begin{bmatrix} \omega_x \\ \omega_z \end{bmatrix} = \begin{bmatrix} V_x/h \\ V_z/h \end{bmatrix}$ and the inertial measurements were therefore used to perform soft lunar landing. We can now write:

$$\begin{cases} a_{ldr_z}(t) = \dot{V}_z = \frac{u_z(t)}{m_{ldr}(t)} - g_{Moon} \\ a_{ldr_x}(t) = \dot{V}_x = \frac{u_x(t)}{m_{ldr}(t)} \end{cases} \tag{18}$$

along with the two virtual control inputs $u_x(t) = u_{th}(t)\sin(\theta(t))$ and $u_z(t) = u_{th}(t)\cos(\theta(t))$.
Let the candidate Lyapunov function $\mathcal{L}_1$ be defined by:

$$\mathcal{L}_1 = \frac{1}{2}\left(h\omega_x - h^*\omega^*_x\right)^2 \tag{19}$$

where h^* and ω^*_x correspond to the height and the ventral OF impinging on the lander during the landing scenario with the optimal control sequences $(u^*_{th},\ u^*_\theta)$ computed offline (see Sect.V). $\mathcal{L}_1$ is always positive ($\mathcal{L}_1 \geq 0$). Its time derivative can then be expressed as follows:

$$\dot{\mathcal{L}}_1 = \left(V_x - V^*_x\right)\left(\dot{V}_x - \dot{V}^*_x\right) \tag{20}$$

where $\dot{V}_x = a_{ldr_x} = \frac{u_x(t)}{m_{ldr}(t)}$.
In the case of a control signal such that:

$$u_x = m_{ldr}\left(\dot{V}^*_x - k_x(t)\left(\omega_x - \omega^*_x\right)\right) \tag{21}$$

where $k_x(t)$ is a strictly positive time varying gain (described below the proof), we obtain:

$$\dot{\mathcal{L}}_1 = \left(V_x - V^*_x\right)\left(-k_x(t)\left(\frac{V_x}{h} - \frac{V^*_x}{h^*}\right)\right) \tag{22}$$

This yields:

$$\dot{\mathcal{L}}_1 = \left(V_x - V^*_x\right)\left(\frac{-k_x(t)}{h}\left(V_x - V^*_x + \frac{\delta h V^*_x}{h^*}\right)\right) \tag{23}$$

where $\delta h = h^* - h$. Lastly:

$$\dot{\mathcal{L}}_1 = -\frac{k_x(t)\sqrt{2}}{h}\left[\sqrt{2}\mathcal{L}_1 + \delta h \omega_x^* \text{sign}\left(V_x - V_x^*\right)\sqrt{\mathcal{L}_1}\right] \quad (24)$$

where $\text{sign}\left(X\right) = \begin{cases} 1 & X \geq 0 \\ -1 & X < 0 \end{cases}$.

Since the reference scenario adopted in this paper focuses on the approach phase from HG (1800m) to LG (10m), the height is always positive $\forall t \geq 0$.

Therefore, even with $(k_x(t),\ h) \geq 0$, a sign study had to be conducted in order to determine the evolution of $\dot{\mathcal{L}}_1$. Several possible cases could occur:

1) $\text{sign}\left(\delta h\right) = \text{sign}\left(V_x - V_x^*\right)$
   It can be seen here that $\dot{\mathcal{L}}_1$ is strictly negative. This means that with $\mathcal{L}_1 = \frac{1}{2}\left(h\omega_x - h^*\omega_x^*\right)^2 = \frac{1}{2}\left(V_x - V_x^*\right)^2 \geq 0$ and $\dot{\mathcal{L}}_1 < 0$, V_x tends asymptotically toward V_x^*.
2) $\text{sign}\left(\delta h\right) \neq \text{sign}\left(V_x - V_x^*\right)$
   Therefore,

$$\dot{\mathcal{L}}_1 = -\frac{k_x(t)\sqrt{2}}{h}\left[\sqrt{2}\mathcal{L}_1 - |\delta h|\,\omega_x^*\sqrt{\mathcal{L}_1}\right] \quad (25)$$

   The sign of $\sqrt{2}\mathcal{L}_1 - |\delta h|\,\omega_x^*\sqrt{\mathcal{L}_1}$ then has to be studied:
   a) $\sqrt{2}\mathcal{L}_1 - |\delta h|\,\omega_x^*\sqrt{\mathcal{L}_1} > 0$, which means:

$$\mathcal{L}_1(t) > \left(\frac{\omega_x^*(t)\,|\delta h(t)|}{\sqrt{2}}\right)^2 \quad (26)$$

   Hence, as long as $\mathcal{L}_1$ is greater than the curve described by $\left(\frac{\omega_x^*(t)|\delta h(t)|}{\sqrt{2}}\right)^2$, $\dot{\mathcal{L}}_1$ will be strictly negative.
   b) $\sqrt{2}\mathcal{L}_1 - |\delta h|\,\omega_x^*\sqrt{\mathcal{L}_1} < 0$, which means:

$$\mathcal{L}_1(t) < \left(\frac{\omega_x^*(t)\,|\delta h(t)|}{\sqrt{2}}\right)^2 \quad (27)$$

   Therefore, as long as $\mathcal{L}_1$ is smaller than the curve described by $\left(\frac{\omega_x^*(t)|\delta h(t)|}{\sqrt{2}}\right)^2$, $\dot{\mathcal{L}}_1$ will be strictly positive.

Up to this point, we have proved that $\mathcal{L}_1$ converge toward $\left(\frac{\omega_x^*(t)|\delta h(t)|}{\sqrt{2}}\right)^2$. Let us now have a look at the system's behavior when we have equality. The latter case will now be studied to explain what the aforementioned convergence means from the physical point of view.

   c) $\sqrt{2}\mathcal{L}_1 - |\delta h|\,\omega_x^*\sqrt{\mathcal{L}_1} = 0$, which means:

$$\mathcal{L}_1(t) = \left(\frac{\omega_x^*(t)\,|\delta h(t)|}{\sqrt{2}}\right)^2 \quad (28)$$

   Since $\mathcal{L}_1 = \frac{1}{2}\left(h\omega_x - h^*\omega_x^*\right)^2$, as long as $\mathcal{L}_1$ is located on the curve described by $\left(\frac{\omega_x^*(t)|\delta h(t)|}{\sqrt{2}}\right)^2$ (which means (28) is verified), we have:

$$|h\omega_x - h^*\omega_x^*| = \omega_x^*\,|\delta h| \quad (29)$$

   Lastly, a trivial sign study has to be conducted on (29). The first case would be $\text{sign}\left(\delta h\right) = \text{sign}\left(h\omega_x - h^*\omega_x^*\right) = \text{sign}\left(V_x - V_x^*\right)$, which is not in keeping with the hypothesis stated above $(\text{sign}\left(\delta h\right) \neq \text{sign}\left(V_x - V_x^*\right))$.
   The only possible solution is then $\text{sign}\left(\delta h\right) \neq \text{sign}\left(h\omega_x - h^*\omega_x^*\right)$ which yields:

$$h\omega_x - h^*\omega_x^* = -\omega_x^*\delta h = \omega_x^* h - \omega_x^* h^* \quad (30)$$

   with $\delta h = h^* - h$, we obtain

$$h\omega_x - h^*\omega_x^* = \omega_x^* h - \omega_x^* h^*$$

   Finally, when (28) is satisfied, this means that $\omega_x = \omega_x^*$.

Although the signs of δh and $\left(V_x - V_x^*\right)$ are unknown and depend on the initial conditions, it was observed in practice that these signs remain unchanged throughout the descent. As can be seen from Fig. 6, at all values of $\delta h_0 \in [-180;\ 180]$, $\mathcal{L}_1(t)$ increases when it is smaller than the curve described by $\left(\frac{|\delta h|\omega_x^*}{\sqrt{2}}\right)^2$ and decreases when it is greater, which means that ω_x tends toward ω_x^*. This theoretical sign study showed that:

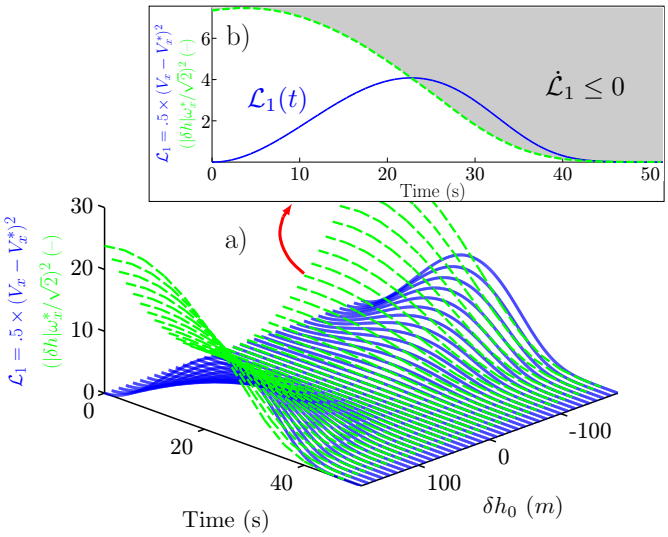

Fig. 6. a) Evolution of the Lyapunov function $\mathcal{L}_1 = \frac{1}{2}\left(h\omega_x - h^*\omega_x^*\right)^2$ (solid blue) for $h_0 = h_0^* \pm 10\%$ and $V_{x_0} = V_{x_0}^* + 0.03$ b) Evolution of the Lyapunov function $\mathcal{L}_1$ (solid blue) versus time with $h_0 = h_0^* - 100$ and $V_{x_0} = V_{x_0}^* + 0.03$

- the control law u_x ensures that V_x tends asymptotically toward V_x^* when there exists a time $t^* > 0$ such that $t \geq t^*$ $\text{sign}\left(\delta h\right) = \text{sign}\left(V_x - V_x^*\right)$,
- the control law u_x ensures that ω_x tends asymptotically toward $\omega_x^*$when there exists a time $t^* > 0$ such that $t \geq t^*$ $\text{sign}\left(\delta h\right) \neq \text{sign}\left(V_x - V_x^*\right)$.

In addition, although the convergence of V_x cannot be ensured in all cases, one can see that the Lyapunov function tends in practice toward 0 (i.e., V_x tends toward V_x^*) with all initial heights as from 1800 m $\pm$ 10%. The insert in Fig. 6 gives a typical example, where $h_0 = h_0^* - 100$ and $V_{x_0} = V_{x_0}^* + 0.03$.

To deal with the vertical dynamics, we apply the same Lyapunov based approach, taking the control signal to be:

$$u_z = m_{ldr}\left(g_{Moon} + \dot{V}_z^* - k_z(t)\left(\omega_z - \omega_z^*\right)\right) \quad (31)$$

Which yields the same sign results and conclusions with:

$$\dot{\mathcal{L}}_2 = -\frac{k_z(t)\sqrt{2}}{h}\left[\sqrt{2}\mathcal{L}_2 + \delta h \omega_z^* \text{sign}\left(V_z - V_z^*\right)\sqrt{\mathcal{L}_2}\right] \quad (32)$$

where $k_z(t)$ is a strictly positive time varying gain (described below the proof). Based on a similar sign study, it can be proved that when $\text{sign}\left(\delta h\right) = \text{sign}\left(V_z - V_z^*\right)$, the control law u_z ensures that V_z tends asymptotically toward V_z^* and when $\text{sign}\left(\delta h\right) \neq \text{sign}\left(V_z - V_z^*\right)$, the control law u_z ensures that ω_z tends asymptotically toward ω_z^*. It can be noted that a feedforward term was included in both u_x and u_z (see (21),(31)). The pre-determined optimal horizontal and vertical acceleration trajectories ($\dot{V}_x^*$ and $\dot{V}_z^*$, respectively) are therefore used in this control scheme.

In order to account for the physical saturation of the delivered control signal $u_{th} = \sqrt{u_x^2 + u_z^2}$, the gains $k_x(t)$ and $k_z(t)$ are expressed as the product of a nominal part (positive constants) and a time varying part $0 < \lambda \leq 1$ preventing saturation so that:

$$\begin{pmatrix} k_x(t) \\ k_z(t) \end{pmatrix} = \lambda \begin{pmatrix} k_x \\ k_z \end{pmatrix} \quad (33)$$

We now have to find an analytical solution for λ. Let recall the expression of the magnitude of the control signal:

$$u_{th} = m_{ldr}\sqrt{\left(\dot{V}_x^* - \lambda k_x \varepsilon_{\omega_x}\right)^2 + \left(g_{Moon} + \dot{V}_z^* - \lambda k_z \varepsilon_{\omega_z}\right)^2}$$

In cases where $u_{th} \leq u_{max}$ (where $u_{max} = 3820$ N), λ is adopted so that $\lambda = 1$ (no saturation is required).

In the saturated case ($u_{th} > u_{max}$), the actually delivered control signal is set to $u_{th} = u_{max}$ and we have to prove that a value of λ exists such that the stability proof holds (there exists a $0 < \lambda \leq 1$ such that positive gains $k_x(t)$ and $k_z(t)$ exist).

We know that when $\lambda = 1$, we have $u_{th} > u_{max}$ (the saturated case). In addition, when $\lambda = 0$, we have $u_{th} = u_{th}^*$ (with no feedback) and we know that $u_{th} = u_{th}^* < u_{max}$ (a 10% margin on the control signal is added in the optimal control problem so that the optimal control sequence does not reach saturation). Since the expression for $u_{th}(\lambda)$ is a continuous function in $\lambda \in]0;1[$, there exists a $\lambda \in]0;1[$ such that:

$$m_{ldr}\sqrt{\left(\dot{V}_x^* - \lambda k_x \varepsilon_{\omega_x}\right)^2 + \left(g_{Moon} + \dot{V}_z^* - \lambda k_z \varepsilon_{\omega_z}\right)^2} = u_{max} \quad (34)$$

Lastly, it can be concluded that $\forall t \geq 0$ there exists a $0 < \lambda \leq 1$ such that the control signal can be saturated ($u_{th} = u_{max}$) if necessary.

It is worth noting that all the optimal signals appearing in the control laws (marked with a *) could be replaced by any pre-computed reference signals, which do not have to be the optimal ones.

B. Pitch control law

The inner control loop is based on a sub-optimal guidance scheme feeding a proportional derivative controller with a feedforward action.

Since the pitch dynamics were defined as a double integrator (2), the control law was designed as follows:

$$u_\theta(t) = u_\theta^{ff}(t) + K_p \varepsilon_\theta(t) + K_d \frac{d}{dt}\varepsilon_\theta(t) \quad (35)$$

where $u_\theta^{ff}(t)$ corresponds to the optimal control sequence $u_\theta^*(t)$ computed in Sec. V and $\varepsilon_\theta(t) = \theta_{meas}(t) - \theta^*(t)$.

Another possible approach would have consisted in defining the reference pitch trajectory based on the control signals u_x and u_z such that $\theta_{ref}(t) = \arctan\left(\frac{u_x}{u_z}\right)$. However, the results obtained using this strategy showed that $\theta_{ref}(t) = \arctan\left(\frac{u_x}{u_z}\right)$ were liable to give a very noisy, non-smooth reference signal (e.g. when $u_z \to 0$). In addition, since the closed-loop system closely matches the optimal OF trajectory, which was defined in keeping with a optimal pitch trajectory, $\theta^*(t)$ was used as the attitude control loop reference signal. In conclusion, this virtual decoupling between the two loops prevents noise from being transmitted from the 6-pixel VMS to the pitch controller while providing a consistent reference pitch trajectory.

Gains K_p and K_d were defined using classical pole placement methods on a double integrator system, thus giving the closed-loop faster dynamics than the outer loop (OF control).

C. Simulation results

The results of the closed-loop simulation performed with PANGU using 2 gimbaled OF sensors show that the GNC strategy implemented with software-in-the-loop constitutes an efficient means of performing soft landing, since the final constraints in terms of the velocity and the attitude are almost met (V_{x_f} is slightly higher than 1 m/s). In this study, the attitude measurements were taken to be perfect throughout the whole simulated descent phase. Well-known drawbacks of IMU devices such as drift and measurement noise extensively studied in the literature are beyond the scope of this paper. Figure 7 shows the landing scenario simulated in closed loop using the sub-optimal guidance strategy, the two decoupled feedback loops in a SIL simulation using PANGU and 2 gimbaled 6-pixel VMSs taking simplified actuator dynamics (as first order systems) and thrust saturation into account.

From Fig. 7.a, Fig. 7.d and Fig. 7.e, the present sub-optimal guidance and control scheme makes it possible to obtain a trajectory ($V_x(t),\ V_z(t),\ x(t),\ h(t),\ \theta(t)$) which is similar to the optimal trajectory computed using non-linear programming methods. In Fig. 7.b, it can be seen that the OF follows the reference signals. Figure 7.c shows the control input (u_{th}), which is very similar to the optimal control sequences presented in Fig. 5.b).

The black dots in this figure indicate the sensor initiation phase. Two seconds before reaching HG, the sensors are switched on. In simulations, the lander is in open loop up to $h = 1800$m. In real landings, however, another GNC strategy would have to be used prior to High Gate.

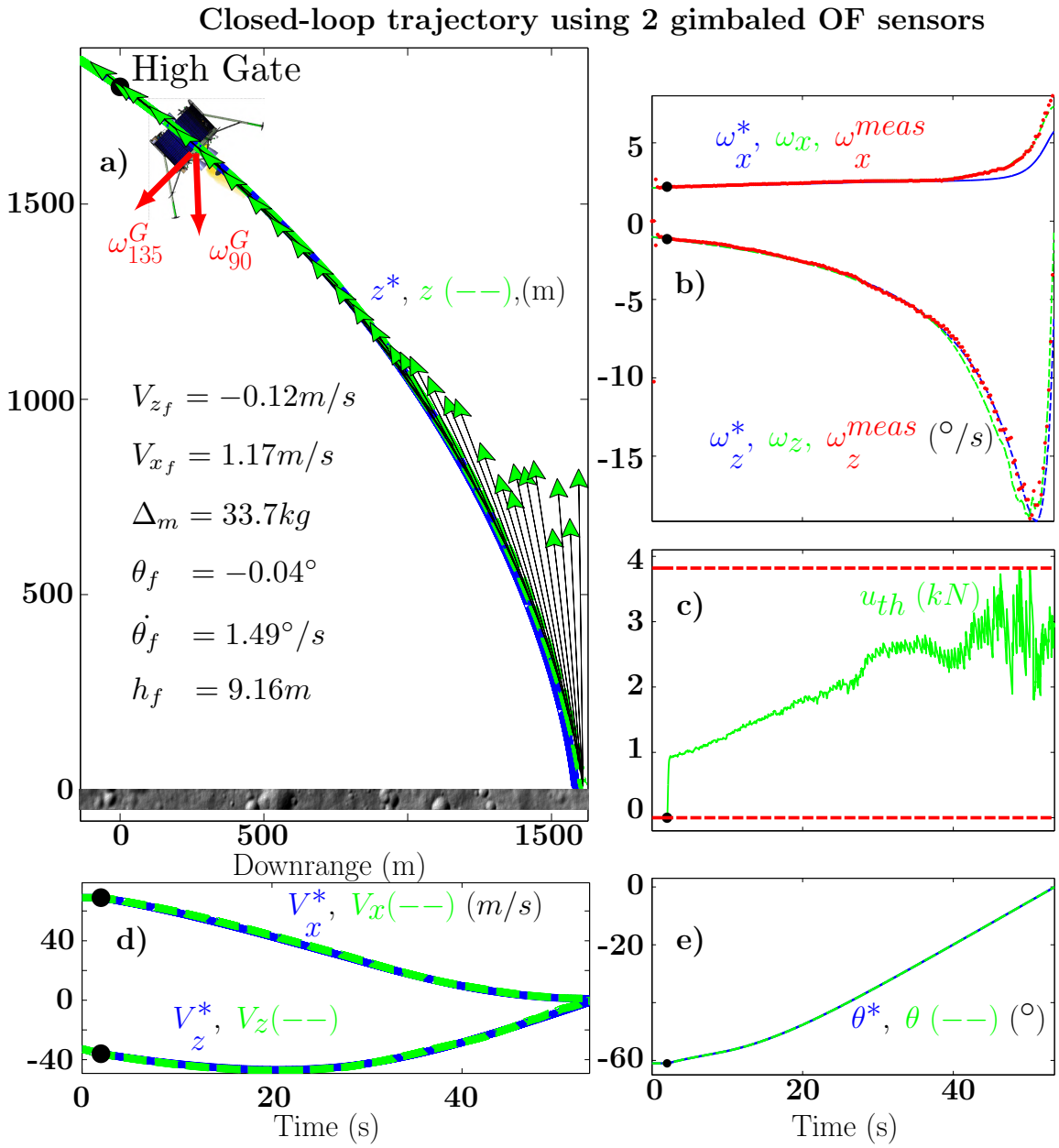

Fig. 7. Closed-loop response from HG to LG in a SIL simulation performed on PANGU using 2 gimbaled OF sensors. a) Height h versus downrange x (green dashed), optimal trajectory $h^*(x)$ (solid blue line), orientation and normalized magnitude of the control input u_{th}. b) Optimal reference OF profiles (dashed black lines), ground-truth OF (solid red lines) and measured OF (dotted blue lines). c) Control sequence $u_{th} = \sqrt{u_x^2 + u_z^2}$. Saturation of the control signal u_{th} is such that 0 N $\leq u_{th} \leq$ 3820 N. d) Velocities V_x, V_z (dashed lines) and optimal references (solid lines). e) Optimal pitch reference trajectory (solid line) and actual pitch (dashed line). Black dots indicate the times at which the lander reaches HG.

Up to this point, we have taken the two 6-pixel VMSs to be gimbaled and therefore to be able to directly measure $\omega_x = \frac{V_x}{h}$ and $\omega_z = \frac{V_z}{h}$ (see (11) and (12)).

In the following section, a linear least squares regression is performed to estimate ω_x and ω_z using 20 OF sensors fixed to the lander's structure, thus doing away with the need to use any gimbaled system.

VII. Non-gimbaled OF sensor set-up

A. Problem formulation

Since the goal pursued here consists in ensuring soft lunar landing and the solution therefore needs to be cost- and weight-saving, it was not proposed to embed a gimbal system onboard the lander. In the presence of sensors fixed to the lander's structure, the OF measurements depend on the pitch angle, which directly affects the distance to the ground in the gaze direction D, as illustrated in Fig. 8.

The control strategy based on the OF regulators described in section VI involved the use of only a few specific OF values, which were of particular interest due to their mathematical expressions: ω_x and ω_z, as defined in (11)-(12). ω_x and ω_z can easily be obtained from $\omega_{90°}$ and $\omega_{135°}$ when they are available, but this is rarely the case. An estimation algorithm is therefore required to approximate the values of ω_x and ω_z

from the OF measurements available at each time step. The main idea here is to increase the number of VMSs on the lander so as to be able to estimate these useful values. To express ω_x and ω_z based on just a few measurements, we implemented and simulated a method involving the use of a linear least squares algorithm using multiple sensors' outputs.

The general expression for the translational OF after the derotation process (i.e. $\omega_\Phi = \omega_T = \omega_{measured} - \omega_R$) is defined as follows:

$$\omega_\Phi = \frac{V}{D}\sin(\Phi) \tag{36}$$

with $\Phi = \alpha + \theta + \gamma$, where $\alpha > 0$ is the fixed angle between the orientation of the OF sensor and the vector $\vec{x_b}$ and $(\theta;\gamma) < 0$.

Figures 8.a-c and Fig. 8.e show the actual low-speed VMS electronic board (Fig. 8.b gives the front view, and Fig. 8.c gives the rear view) and custom-made packaging (Front view in Fig. 8.a, top view in Fig. 8.e), Fig. 8.d gives the notations, reference frames and illustrates the previous statement $\Phi = \alpha + \theta + \gamma$ about an enhanced OF sensor configuration. Figures 8.f-g show the lander equipped with 20 VMSs installed $5°$ apart.

We now have to find the equation that describes the evolution of the OF at a given ground height h and velocity V, depending on the gaze direction (defined by α and θ). Assuming the presence of a flat terrain, the distance to the ground in the gaze direction can be expressed as follows:

$$D = \frac{h}{\cos(\alpha - \frac{\pi}{2} + \theta)} = \frac{h}{\sin(\alpha + \theta)} \tag{37}$$

Finally, we obtain:

$$\omega_{\alpha+\theta}(t) = \frac{V(t)}{h(t)}\sin(\alpha + \theta(t))\sin(\alpha + \theta(t) + \gamma(t)) \tag{38}$$

where α and θ are initially given and measured parameters, respectively.

Equation (38) describes the evolution of the OF in the case of a sensor oriented at the angle α. It is worth noting that this is a nonlinear time varying expression.

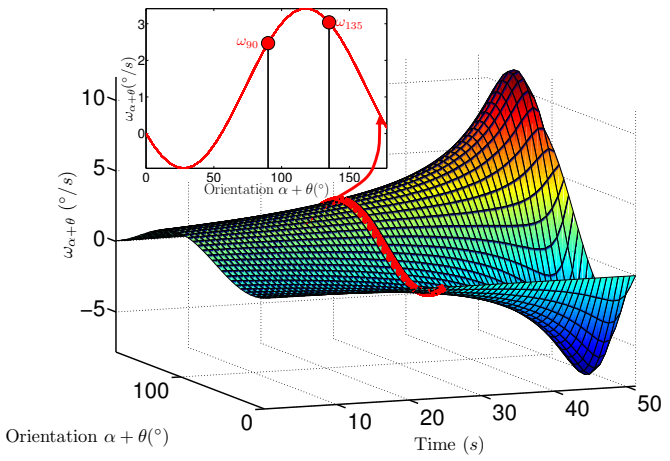

Fig. 9. a) Evolution of $\omega_{\alpha+\theta}(t)$ with time in the case of the optimal reference descent trajectory presented in Fig. 5. b) OF characteristics depending on the gaze direction at $t = 25.72$ s (i.e. for $V_x = 29.25$ m/s, $V_z = -44.52$ m/s and $h = 675.12$ m). Values of particular interest $\omega_{90°}$ and $\omega_{135°}$ are given in red.

Figure 9 gives the evolution of the OF $\omega_{\alpha+\theta}(t)$ with time during the optimal reference descent trajectory presented in Fig. 5 with $\theta(t_i) = 0$ and $\alpha \in [0;\pi]$ (the boundary values correspond to an infinite ground). The insert in the Fig. 9 shows the values of particular interest $\omega_{90°}$ and $\omega_{135°}$ at time t_i. It is worth noting that from one time step to the next, the number of ground-oriented OF sensors is liable to vary, which affects the magnitude and hence the difficulty of the problem.

Assuming the presence of a flat ground, the OF sensor fixed at the angle α will no longer be ground-oriented when the following inequality is not satisfied:

$$-\alpha \leq \theta \leq -\alpha + \pi \tag{39}$$

It is necessary to identify all the OF sensors that do not satisfy the ground orientation condition (39). Figure 10 gives an overview of the evolution of the orientation of each OF sensor depending on the pitch angle. Only the OF sensors oriented between $0°$ and $180°$ (between the two dash-dotted black lines in Fig. 10) will provide useful OF measurements, since they are oriented toward the ground. Under real-life conditions, these boundaries have to be tightened due to the fact that the lunar radius is not infinite. The OF at the Focus of Expansion (FoE) is always null, and in the immediate neighborhood, it is approximately null: there is therefore no point in having any OF sensors oriented in this direction. The red dashed line in Fig. 10 gives the orientation of the FoE defined by $\tan^{-1}\left(\frac{V_z}{V_x}\right)$.

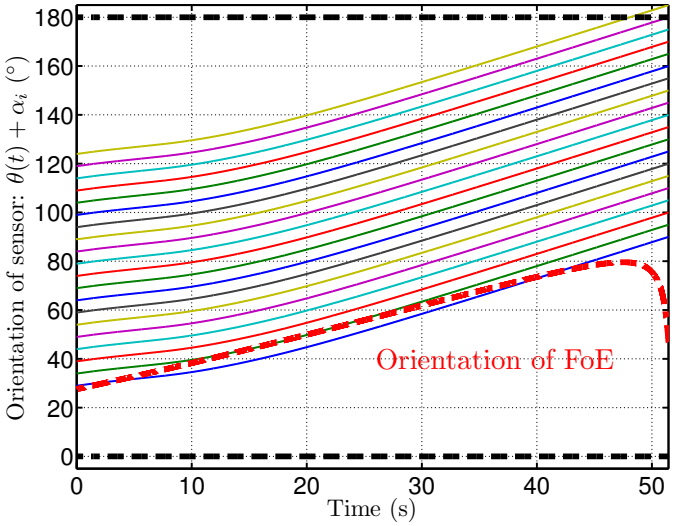

Fig. 10. Evolution of the OF sensor's orientation $\theta(t)+\alpha_i$ during a reference descent trajectory in a set-up including 20 OF sensors oriented every $5°$.

It is worth noting that in this configuration, at least 19 out of the 20 sensors are pointing in an appropriate direction at any time, i.e., in a ground-oriented direction which is far enough from the FoE.

Equation (39) is checked in the case of each OF sensor by applying a ground-oriented sensor selection algorithm at each time step.

During the PANGU simulations, OF sensors were sky-oriented even when the condition described in (39) was met, because of the size of the Digital Elevation Model, which is

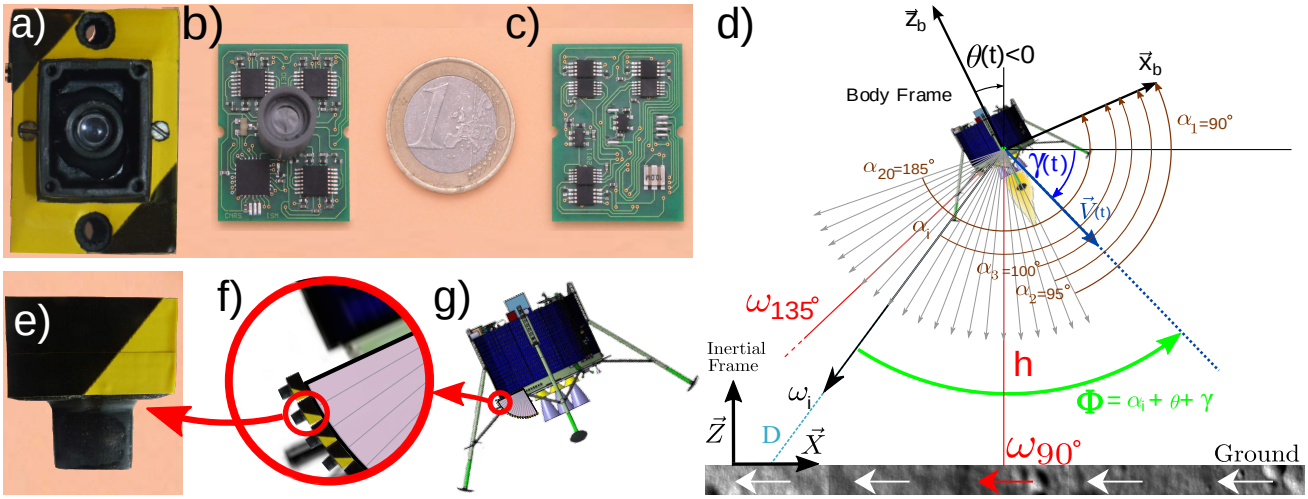

Fig. 8. a) Front view of the custom-made protective case of the VMS. b)-c) Front and back view of the low-speed 6-pixel VMS. From [35]. d) Lander with 20 embedded VMSs with a non-null pitch angle: $\omega_i = \frac{V}{D}\sin(\alpha_i + \theta + \gamma)$, $(\theta;\gamma) < 0$. e) Top view of the VMS. f) Zoom on the proposed implementation of the VMSs fixed to the lander's structure (1 sensor every 5° from 90° to 185°). g) Overall view of the lander equipped with 20 embedded VMSs approaching the lunar ground.

limited to $2^n \times 2^n$m (n is usually set at 12 or 13 depending on the sensor configuration). Without knowing either the height or the absolute position on the Digital Elevation Model, geometric criteria cannot be used to determine which OF sensors are pointing out of the map. Whenever a 6-pixel OF sensor is sky-oriented, its photodiodes' raw visual signals decrease to approximately zero (PANGU generates stars, which trigger a residual visual signal): this OF sensor is then rejected as long as $\sum_{i=1}^{6} ph_i < threshold$, where ph_i denotes the ith photodiode signal ($threshold$ is set experimentally at a higher value than the sum of six photodiodes oriented toward a sky full of stars).

B. Least squares estimation

It was then proposed to estimate both ω_x and ω_z based on a limited number of OF measurements giving results which were at least as accurate as those which would have been obtained with a gimbaled mounted sensor subjected to the same measurement dispersion. Instead of estimating $(\omega_{90°}, \omega_{135°})$ to compute $\hat{\omega}_x$ and $\hat{\omega}_z$, an expression for the OF measurement can be obtained for every α_i in terms of $\omega_x = \frac{V_x(t)}{h(t)}$ and $\omega_z = \frac{V_z(t)}{h(t)}$.

$$\omega_{\alpha_i+\theta(t)} = \frac{1}{2}\begin{bmatrix} 1-\cos\left(2\left(\alpha_i+\theta(t)\right)\right) & \sin\left(2\left(\alpha_i+\theta(t)\right)\right)\end{bmatrix}\begin{bmatrix}\frac{V_x(t)}{h(t)}\\ \frac{V_z(t)}{h(t)}\end{bmatrix} \quad (40)$$

It is therefore theoretically possible to deduce ω_x and ω_z based on only two measurements as long as the matrix is invertible:

$$\begin{bmatrix}\omega_x\\ \omega_z\end{bmatrix} = \frac{1}{2}\begin{bmatrix}1-\cos(2(\alpha_1+\theta)) & \sin(2(\alpha_1+\theta))\\ 1-\cos(2(\alpha_2+\theta)) & \sin(2(\alpha_2+\theta))\end{bmatrix}^{-1}\begin{bmatrix}\omega_{\alpha_1+\theta}\\ \omega_{\alpha_2+\theta}\end{bmatrix} \quad (41)$$

By increasing the number of measurements, the estimated output can be improved and null determinant issues can be avoided. However, since the matrix will no longer be a square matrix, the Moore-Penrose pseudoinverse defined as $A^+ = (A^TA)^{-1}A^T$ can be used to obtain an estimation of $\begin{bmatrix} V_x(t)/h(t) & V_z(t)/h(t)\end{bmatrix}^T$.

$$\begin{bmatrix}\hat{\omega}_x^{LS}(t)\\ \hat{\omega}_z^{LS}(t)\end{bmatrix} = \frac{1}{2}A^+\begin{bmatrix}\omega_{\alpha_1+\theta}(t)\\ \vdots\\ \omega_{\alpha_N+\theta}(t)\end{bmatrix} \quad (42)$$

where

$$A = \begin{bmatrix}1-\cos(2(\alpha_1+\theta(t))) & \sin(2(\alpha_1+\theta(t)))\\ \vdots & \vdots\\ 1-\cos(2(\alpha_N+\theta(t))) & \sin(2(\alpha_N+\theta(t)))\end{bmatrix} \quad (43)$$

and the upper script LS denotes the output of the linear least squares algorithm. It is worth noting that the expressions described in (11) and (12) correspond to a specific case of the least squares formulation, where two gimbaled sensors are oriented toward 90° and 135° from the local horizontal.

C. Results

A study of the standard deviation of the error was conducted in order to determine the number of OF sensors to be used in the least squares algorithm. This basically amounts to making a trade-off between the accuracy required in the estimation and the complexity and weight of the embedded sensors and the algorithm. Figure 11.a shows the standard deviation of the error for all possible implementations from 2 sensors to 50. The noise added to the measurements consists of pseudo-random values based on the standard uniform distribution in the interval $[-3°/s, 3°/s]$.

To make the number of sensors selected at least as accurate as that obtained with the gimbaled solution, the standard deviation error of the $\hat{\omega}_x^{LS}$, $\hat{\omega}_z^{LS}$ estimated using N non-gimbaled OF sensors was compared with the result obtained using a direct method of estimation based on 2 gimbaled sensors $\omega_{90°}^G$ and $\omega_{135°}^G$ (see (11)-(12)), where the upper script G denotes the output of a gimbaled sensor. As a design

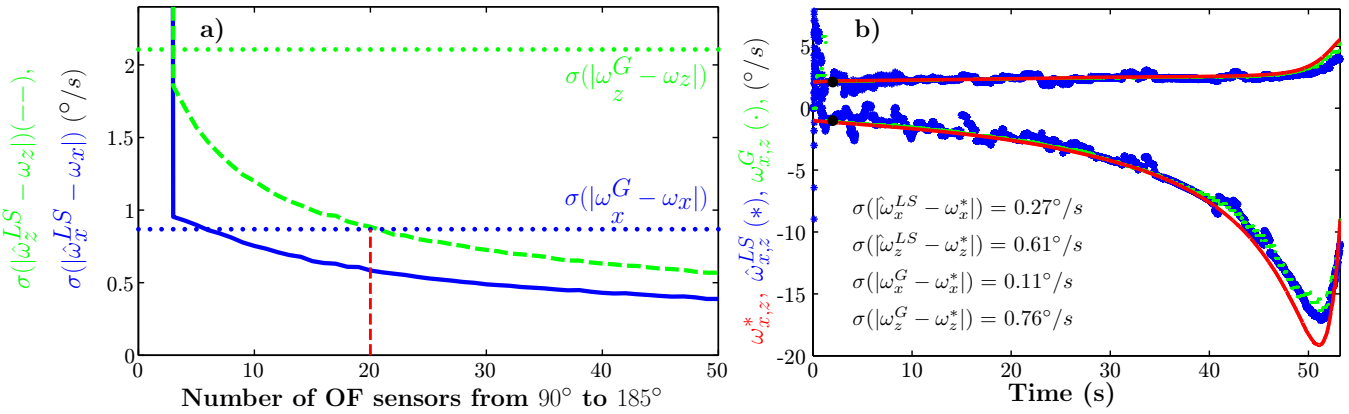

Fig. 11. a) Standard deviation of the error between ω_x and $\hat{\omega}_x^{LS}$ (blue) (ω_z and $\hat{\omega}_z^{LS}$ (green)) versus the number of OF sensors equally spaced between 90° and 185° during an optimal reference descent trajectory. The dashed horizontal line gives the standard deviation of the error of the estimates obtained using 2 gimbaled OF sensors: $\omega_x^G = \omega_{90°}^G$ and $\omega_z^G = \omega_{90°}^G - 2\omega_{135°}^G$ where $\omega_{i°}^G$ denotes the measurement obtained with an OF sensor oriented downward at $i°$ from the local horizontal. A total number of 20 sensors (placed 5° apart) therefore constitutes an acceptable compromise between the accuracy requirements and the complexity of the implementation. b) Validation of the least squares algorithm with a 20 OF sensor configuration. Comparison between the true values of ω_x, and ω_z during a descent trajectory (red) and the estimated values $\hat{\omega}_x^{LS}$ and $\hat{\omega}_z^{LS}$ (blue) and the values that would have been measured with a sensor mounted on a gimbal system subjected to the same noise level(s) ω_x^G and ω_z^G (green). Black dots indicate the times at which the lander reaches HG.

criterion for setting the number of OF sensors, the standard deviation of the error in the least squares estimation had to be of the same order of magnitude as the value obtained in the case of gimbaled sensors.

The results of the simulation showed that the use of the linear least squares algorithm to estimate $\hat{\omega}_x^{LS}$ and $\hat{\omega}_z^{LS}$ in a setup including 20 OF sensors separated by a fixed angle is a suitable procedure. The angle between each of the sensors was set experimentally at 5°, from $\alpha_{min} = 90°$ up to $\alpha_{max} = 185°$. With this configuration, it can be seen from Fig. 11.a that $\sigma\left(\left|\hat{\omega}_x^{LS} - \omega_x\right|\right) = 0.47°/s$ is below $\sigma\left(\left|\omega_x^G - \omega_x\right|\right) = 0.87°/s$ and $\sigma\left(\left|\hat{\omega}_z^{LS} - \omega_z\right|\right) = 0.89°/s$ is way below $\sigma\left(\left|\omega_z^G - \omega_z\right|\right) = 2.11°/s$ and very near $\sigma\left(\left|\hat{\omega}_x^G - \omega_x\right|\right) = 0.87°/s$ ($0.02°/s$ higher), which means that 20 OF sensors is a number giving an appropriate trade-off when the non-gimbaled method is used to estimate ω_x and ω_z. This procedure was then tested using PANGU: this simulation was run in open loop on the optimal scenario in order to test the validity of the navigation solution. The results obtained with the least squares algorithm using 20 non-gimbaled OF sensors on PANGU and the results of the estimation based on 2 gimbaled OF sensors are given in Figure 11.b.

It can be seen from Fig. 11.b as expected, that the standard deviation of the error with $\hat{\omega}_x$ was reasonably similar to the value obtained with the gimbaled measurements ($\sigma\left(\left|\hat{\omega}_x^{LS} - \omega_x\right|\right) = 0.27°/s$ versus $\sigma\left(\left|\omega_x^G - \omega_x\right|\right) = 0.11°/s$) and that the standard deviation of the error with $\hat{\omega}_z^{LS}$ was even better than in the case of gimbaled measurements ($\sigma\left(\left|\hat{\omega}_z^{LS} - \omega_z\right|\right) = 0.61°/s$ versus $\sigma\left(\left|\omega_z^G - \omega_z\right|\right) = 0.76°/s$). Differences with the results of the theoretical study presented in Fig. 11.a are due to the fact that the actual VMS noise (occurring with the simulated VMS on PANGU generated images) differed from the pseudo-random values based on the standard uniform distribution. It can be noted that $\sigma\left(\left|\hat{\omega}_z^{LS} - \omega_z\right|\right)$ is slightly higher than $\sigma\left(\left|\omega_x^G - \omega_x\right|\right)$. These results again confirm that the estimation of ω_x and ω_z via a least squares algorithm and 20 non-gimbaled 6-pixels VMS is sufficiently accurate in comparison with that obtained with the 2 gimbaled OF sensor method.

A well-known drawback of the least squares method of estimation is its sensitivity to noise. Even with noisy measurements, however, the linear least squares algorithm is accurate enough in the present context. Other estimation techniques could be used in this framework. One possibility which comes to mind is to use an improved least squares regression method using weighting matrices, iterative methods or nonlinear least squares, but this method failed to improve the estimates obtained in the preliminary investigations (not shown).

VIII. Complete GNC simulation using PANGU

Lastly, the full GNC strategy presented in this paper was simulated using PANGU. The main features on which this strategy is based are:

- sub-optimal OF and pitch guidance with respect to the fuel consumption,
- two decoupled control loops for performing OF and pitch reference tracking
- and the non-gimbaled OF fusion algorithm for estimating ω_x and ω_z using 20 OF sensors in SIL simulations.

In the simulation 20 OF sensors are fixed to the lander's structure every 5° at an angle of $\alpha \in [90°; 185°]$.

Table II gives the results of the SIL simulation performed in closed-loop with PANGU using 2 gimbaled versus 20 non-gimbaled OF sensors and shows the relative errors in the fuel consumption, vertical velocity braking and horizontal velocity braking:

Relative error computation

$$\varepsilon_{\Delta m} = \frac{\Delta m - \Delta m^*}{\Delta m^*}, \quad \varepsilon_{V_{(x,z)}} = \frac{(V_{(x,z)_0} - V_{(x,z)_f})(V^*_{(x,z)_0} - V^*_{(x,z)_f})}{V^*_{(x,z)_0} - V^*_{(x,z)_f}}.$$

This simulation shows that the closed-loop control strategy almost meets the demanding final constraints despite the

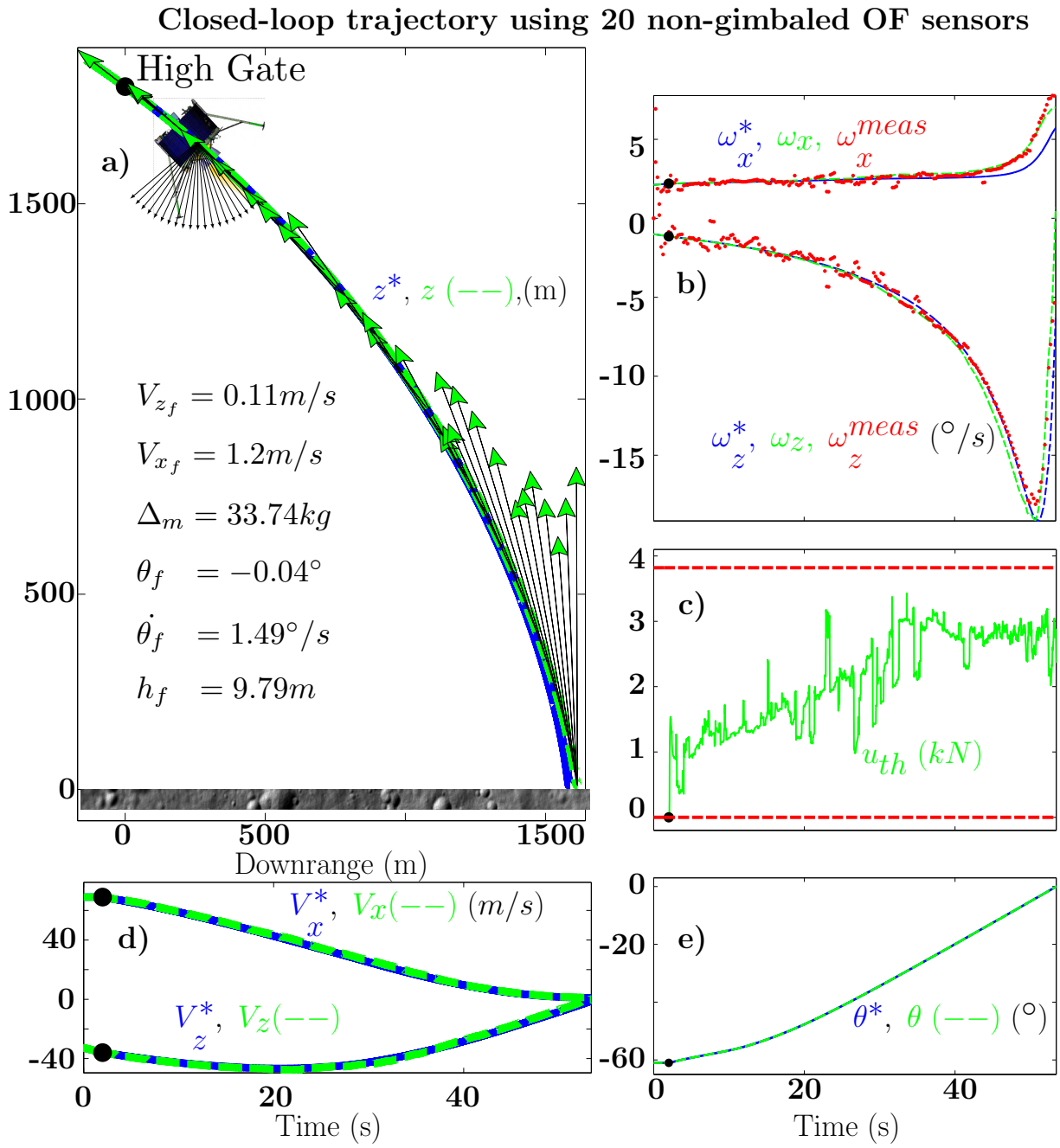

Fig. 12. Closed-loop response from HG to LG obtained in a SIL simulation on PANGU using 20 non-gimbaled OF sensors. a) Height h versus downrange x, orientation and normalized magnitude of the control input u_{th}. b) Measured OF (red dotted lines), ground-truth OF (dashed green lines) and optimal reference OF profile (blue solid lines). c) Control sequence $u_{th} = \sqrt{u_x^2 + u_z^2}$. Saturation of the control signals u_{th} was such that 0 N $\leq u_{th} \leq$ 3820 N. d) Velocities V_x, V_z. e) Pitch reference trajectory (solid line) and actual pitch signal. Black dots indicate the times at which the lander reaches HG.

decoupling of the two control loops, the control input transformation $\left(u_{th} = \sqrt{u_x^2 + u_z^2}\right)$ and the input control saturation.

In addition, simulations performed with 2 gimbaled (Fig. 7) and 20 non-gimbaled (Fig. 12) OF sensors yielded practically the same results at LG, which confirms the validity of our new navigation strategy based on OF sensors fixed to the structure. Figure 12 gives the results obtained on PANGU using the linear least squares algorithm. Figure 12.a gives the trajectory taken and the final conditions obtained at LG. It can be seen that the vertical velocity (Fig. 12.e along with the horizontal velocity) and the pitch angle (Fig. 12.f) met the final constraints. The horizontal velocity was still slightly higher than necessary: $V_{x_f} = 1.2m/s$, which amounts to a 0.3% error in the expected braking (from 69m/s at HG to 1m/s at LG). In terms of the fuel consumption, 33.74kg of propellant was consumed, which amounts to only 0.51% more than in the optimal open-loop control case. The input signals in Fig. 12.d are quite far from the upper saturation point (except during the last few seconds); and the output of the linear least squares algorithm run using the 20 bidirectional low speed OF

TABLE II
COMPARISON BETWEEN FINAL CONDITIONS IN THE OPTIMAL OPEN LOOP CONTROL AND SUB-OPTIMAL CLOSED-LOOP SIMULATIONS WITH PANGU (RELATIVE ERRORS IN THE FUEL CONSUMPTION AND VELOCITIES WITH RESPECT TO THE OPTIMAL TRAJECTORY ARE PRESENTED).

	Optimal computed trajectory in terms of the fuel consumption (u_x^*, u_z^*)	Closed-loop response with 2 gimbaled OF sensors oriented at angles of 90° and 135°	Closed-loop response with non-gimbaled 20 OF sensors oriented every 5°
h_f (m)	10	9.16	9.79
x_f (m)	1585	1610	1614
Δm (kg)	33.57	*33.7* (0.39%)	*33.74* (0.51%)
V_{x_f}(m/s)	1	*1.17* (-0.25%)	*1.2* (-0.29%)
V_{z_f} (m/s)	-1	*-0.12* (2.51%)	*0.11* (3.17%)
θ_f (°)	0	*-0.04*	*-0.04*
$\dot{\theta}_f$ (°/s)	1.49	1.49	1.49

sensors as shown in Fig. 12.b-c is quite smooth. In conclusion, the present results show that our sub-optimal GNC approach based on the use of non-gimbaled bio-inspired OF sensors meets the demanding final constraints at LG without any need for linear velocity or altitude data.

IX. CONCLUSION

The novel GNC solution to the complex challenge of autonomous lunar landing presented here was achieved using only an IMU and insect inspired visual motion sensors. This solution involving the use of lightweight sensors might also be used as a backup GNC solution in the case of main sensors failure.

This study shows that optimal OF and pitch trajectories in terms of the fuel consumption can be obtained from the optimal control sequence computed using nonlinear programming methods in the lander's dynamic model. The optimal profiles can be fed as reference signals to the two decoupled loops driving the translational/expansional OF (ω_x and ω_z) and the attitude (i.e. the pitch angle). In this new approach to the problem of OF based landing, which has been widely studied in the literature, the entire OF and pitch profiles are determined in order to follow the optimal trajectory during the descent instead of taking an arbitrary constant reference OF value or one dictated by the objectives.

The next step will consist in increasing the complexity of the model used to deal with the optimal control problem, using a 3-D set-up (a 6 degree of freedom (DOF) configuration). Adopting planar motion for planetary landing in the case of a planet with atmosphere such as Mars would be a strong assumption. Since the wind gusts on Mars might induce strong lateral translation and rotation movements, the 6-DOF setup is mandatory even at this stage in the design process. There exist no external phenomena on the moon liable to create very strong motion on the roll, yaw and e_y axes. Thrusters' manufacturing flaws and misalignments could result in small movements (on the roll, yaw and e_y axes) that might be taken care of by an attitude control designed to keep the roll and yaw angles (and/or angular rates) at a zero reference value throughout the descent. Null yaw and roll angles (and angular rates) keep the y-motion down to zero, which means that the planar case would correspond to a full 6-DOF configuration.

However, as it is, our application could be sensitive to small angular roll and yaw motions. The time of travel scheme assesses the OF by computing the difference between the times at which two adjacent photodiodes detect a contrast, assuming that the contrast is moving in a straight line. In the case of lateral motion, contrasts are no longer moving in straight lines, which could add some bias to the measurements. If we go one step further, we could imagine hazard avoidance strategies that could be performed during the approach phase. Avoidance maneuvers might require creating strong lateral motion to move from one landing site to another. It is therefore mandatory to provide the GNC solution with 6-DOF abilities in the following design steps. Using sensors of this kind, this could be achieved by increasing the number of pixels and adopting matrix-shaped photoreceptors.

In order to further improve the robustness of this control strategy to initial uncertainties, a set of optimal reference trajectories could be calculated offline and the most suitable one could be chosen as soon as the lander reaches High Gate, since the uncertainty about the initial OF is mainly due to uncertainty about the initial height. As previously discussed, the guidance scheme could be improved by adding a final constraint on the downrange. In addition to the bank of reference trajectories, this should make it possible to achieve roughly the same level of accuracy as that observed in the present case: landing within $\pm$30m of the optimal landing site, which would correspond to making the GNC strategy capable of dealing with pinpoint landing.

Even with an elementary control scheme based on a non-linear controller, the performances obtained here were similar to the optimal OF reference values and hence to the optimal landing profile. The closed-loop fuel consumption showed that the objectives in terms of the fuel costs and the velocities are almost met (the horizontal velocity is 0.2m/s higher than the objective at LG). It is now planned to further improve the control design in terms of the control allocation and the controllers themselves to prevent the occurrence of decoupling between the OF and the pitch feedback loop. Here we have provided theoretical proof of the asymptotic convergence of the OF and that of the velocities with the reference values in the nonlinear system.

The second major improvement made in this study was the use of a non-gimbaled sensor setup. Instead of using a bulky gyro-stabilized system, which is not feasible with these lightweight sensors, we introduced a new method of fusion using 20 sensors oriented in fixed directions to extract the same information as that which can be obtained with a heavy gimbaled sensor system. These sensors are used to

accurately determine the translational and expansional OF (ω_x and ω_z). The results obtained show that thanks to the use of a suitable number of sensors, the values of $\left(\hat{\omega}_x^{LS},\, \hat{\omega}_z^{LS}\right)$ estimated have similar standard deviations of the error as those $\left(\omega_x^G, \omega_z^G\right)$ obtained using two gimbaled OF sensors measuring $(\omega_{90^\circ},\ \omega_{135^\circ})$ subjected to the same noise levels. This strategy basically amounts to making a trade-off between the accuracy of the estimation and the complexity of the physical implementation (and the weight of the system). We have focused here on the methodological aspects of the solution, and this numerical application was based on a compromise between the computational cost and the estimation accuracy, which can be adapted to the application in question. The mathematical formulation of the problem is presented above and the solution obtained was implemented for the first time to our knowledge with such minimalistic sensors.

One of the main advantages of this distributed OF sensor configuration is that if one VMS failure occurs, the solution will keep on functioning, giving slightly lower performances but without jeopardizing the success of the entire landing, contrary to what occurs with classical solutions based on a single main sensor.

The next step will be to develop a theoretical approach for determining the optimal orientation, spacing and number of sensors required to ensure accurate estimates. Thanks to the light weight of our bio-inspired sensors, which weigh only about 2.8g despite the relatively large number of OF devices used, the present solution is still much lighter than the traditional sensor suite used to meet this GNC challenge.

This approach should therefore constitute a promising candidate for future lunar exploration missions. Every constitutive block of the GNC solution was found to be efficient in a SIL simulation involving the actual VMS code and the use of simulated images of the lunar ground generated by PANGU software.

In conclusion, the results presented here provide a promising answer to the challenge of designing means of handling the autonomous approach phase in terms of the guidance, navigation, and control of a lunar lander using the 6-pixel insect-inspired sensors mounted onboard, which were validated here using simulated images of the lunar ground.

ACKNOWLEDGEMENTS

We thank the editor and the two anonymous reviewers for their constructive comments, which helped us to greatly improve the manuscript. We are most grateful to P. Mouyon, S. Viollet and G. Jonniaux for their fruitful suggestions and comments during this study. We thank J. Blanc for improving the English manuscript. This research work was co-funded by CNRS Institutes (Life Science; Information Science; Engineering Science and Technology), the Aix-Marseille University, the European Space Agency, ONERA - the French Aerospace Lab - , Airbus Defence and Space (previously named ASTRIUM EADS), and ESA (European Space Agency) under the Networking/Partnering Initiative program (NPI) for advanced technologies for space.

REFERENCES

[1] Cheng, Y. and Ansar, A. In *IEEE International Conference on Robotics and Automation (ICRA)*, 1573 – 1578, Apr. (2005).
[2] Janschek, K., Tchernykh, V., and Beck, M. In *AIAA Guidance, Navigation, and Control Conference and Exhibit*, (2006).
[3] Flandin, G., Polle, B., Frapard, B., Vidal, P., Philippe, C., and Voirin, T. In *32nd Annual AAS Rocky Mountain Guidance and Control Conference*, (2009).
[4] Mourikis, A., Trawny, N., Roumeliotis, S., Johnson, A., Ansar, A., and Matthies, L. *IEEE Transactions on Robotics* **25**(2), 264 –280 Apr. (2009).
[5] Strandmoe, S., Jean-Marius, T., and Trinh, S. In *AIAA Guidance, Navigation, and Control Conference and Exhibit* (, Portland, OR, AIAA-99-4154, 1999).
[6] Parkes, S., Dunstan, M., Matthews, D., Martin, I., and Silva, V. In *Data Systems in Aerospace (DASIA),* Harris, R., editor, 18.1 (, Prague, Czech Republic, 2003).
[7] Franceschini, N., Riehle, A., and Nestour, A. *Facets of vision*, chapter 17: Directionally selective motion detection by insect neurons, 360–390. Springer (1989).
[8] Franceschini, N., Pichon, J., and Blanes, C. *Philosophical Transactions of the Royal Society of London* **337**, 283–294 (1992).
[9] Ruffier, F. and Franceschini, N. *Robotics and Autonomous Systems* **50**, 177–194 (2005).
[10] Expert, F., Viollet, S., and Ruffier, F. *Journal of Field Robotics* **28**, 529–541 (2011).
[11] Reichardt, W. *Processing of optical data by organisms and machines, International School of Physics "Enrico Fermi": Course XLIII, 1968, Academic Press* , 465 – 493 (1969).
[12] Srinivasan, M. *Physiological Reviews* **91**(2), 413–460 (2011).
[13] Garratt, M. and Chahl, J. *Journal of Field Robotics* **25**, 284–301 (2008).
[14] Hérissé, B., Hamel, T., Mahony, R., and Russotto, F. *Autonomous Robots* **29**(3-4), 381–399 (2010).
[15] Barrows, G. and Neely, C. In *SPIE : Critical technologies for the future of computing*, volume 4109, 52–63 (, San Diego, CA, USA, 2000).
[16] Griffiths, S., Saunders, J., Curtis, A., Barber, B., McLain, T., and Beard, R. *IEEE Robotics & Automation Magazine* **13**, 34–43 (2006).
[17] Ruffier, F. and Franceschini, N. In *IEEE/RSJ International Conference on Intelligent Robots and Systems (IROS)*, 1266–1273. IEEE, (2008).
[18] Beyeler, A., Zufferey, J., and Floreano, D. In *European Micro Aerial Vehicle Conference (EMAV)*, volume 27 (, Delft, Nederlands, 2009).
[19] Kendoul, F., Nonami, K., Fantoni, I., and Lozano, R. *Autonomous Robots* **27**, 165–188 (2009).
[20] Hérissé, B., Hamel, T., Mahony, R., and Russotto, F.-X. *IEEE Transactions on Robotics* **28**(1), 77 –89 Feb. (2012).
[21] Conroy, J., Gremillion, G., Ranganathan, B., and Humbert, J. *Autonomous Robots* **27**, 189–198 (2009).
[22] Hyslop, A. and Humbert, J. *Journal of guidance, control, and dynamics* **33**(1), 147–159 (2010).
[23] Shoemaker, M. and S., H. *Journal of Guidance, Control, and Dynamics* **36:3**, 710–720 (2013).
[24] Valette, F., Ruffier, F., Viollet, S., and Seidl, T. In *International Conference on Robotics and Automation (ICRA)*, 2253–2260, (2010).
[25] Medici, V., Orchard, G., Ammann, S., Indiveri, G., and Fry, S. Technical report, ESA, (2010).
[26] Parkes, S., Martin, I., and Dunstan, M. In *8th International Conference on Space Operations (2004)*, 1–10 (, Montréal, Canada, 2004).
[27] Dubois-Matra, O., Parkes, S., and Dunstam, M. In *21st International Symposium on Space Flight Dynamics (ISSFD)* (, Toulouse, France, 2009).
[28] Izzo, D., Weiss, N., and Seidl, T. *Journal of Guidance, Control, and Dynamics* **34**, 1383–1395 (2011).
[29] Izzo, D. and de Croon, G. *Journal of Guidance, Control, and Dynamics* **35 (4)**, 1362–1367 (2011).
[30] de Croon, G. and Izzo, D. In *23rd International Symposium on Space Flight Dynamics (ISSFD)*, (2012).
[31] Izzo, D. and de Croon, G. In *Proceedings of the EuroGNC 2013, 2nd CEAS Specialist Conference on Guidance, Navigation & Control, Delft University of Technology*, 91–107 (, Delft, The Netherlands, 2013).
[32] Jean-Marius, T. and Strandmoe, S. Technical report, AEROSPATIAL, Espace et Défense, Les Mureaux-France. ESA, ESTEC, (1998).
[33] Sabiron, G., Chavent, P., Burlion, L., Kervendal, E., Bornsclegl, E., Fabiani, P., Raharijaona, T., and Ruffier, F. In *Proceedings of the EuroGNC 2013, 2nd CEAS Specialist Conference on Guidance, Navigation & Control, Delft University of Technology*, 993–1011 (, Delft, The Netherlands, 2013).

[34] Roubieu, F., Expert, F., Sabiron, G., and Ruffier, F. *Sensors Journal, IEEE* **13**(3), 1025–1035 (2013).
[35] Sabiron, G., Chavent, P., Raharijaona, T., Fabiani, P., and Ruffier, F. In *IEEE International Conference on Robotics and Automation (ICRA)*, (2013).
[36] Cheatham, D., Bennett, F., and Branch, T. In *Proceedings of the Apollo Lunar Landing Mission Symposium*, (1966).
[37] Jean-Marius, T. and Trinh, S. Technical Report RM-TN-00-18-AS/M, Aérospatiale Espace & Défense, (1999).
[38] Koenderink, J. and Doorn, A. *Biological Cybernetics* **56**, 247–254 (1987).
[39] Argyros, A., Tsakiris, D., and Groyer, C. *Robotics Automation Magazine* **11**(4), 21 – 30, 68 Dec. (2004).
[40] Falugi, P., Kerrigan, E., and Van Wyk, E. *Imperial College London Optimal Control Software User Guide (ICLOCS)*. Department of Electrical Engineering, Imperial College London, London, UK, (2010).

Guillaume Sabiron received the M.Sc degree in Control Theory, Electronics, and Computer Science from Grenoble Institute of Technology, France. He obtained his Ph.D. degree from ISAE Supaero in Toulouse, France. His current research interests include GNC system for lunar landing based on optic flow. His Ph.D. was supported jointly by ONERA, the European Space Agency, Airbus Defence and Space and the Institute of Movement Science (CNRS / Aix Marseille University) in Marseille, France.

Thibaut Raharijaona received the M.Sc degree in Engineering, automatics and signal processing from the school of Engineering Telecom Physique Strasbourg. He obtained his Ph.D. degree in control engineering from Paris-Sud University at the department of Automatics of Suplec in November 2004. He is currently lecturer in the Biorobotics Department, Institute of Movement Science, CNRS/Aix-Marseille University, Marseille. His current research interests include multi-objective control system design, biomimetics robotics, guidance and control of UAVs, lunar landing and aerospace applications.

Laurent Burlion received in 2003 the M.Sc degree in Control Theory at the IRRCyN in Nantes and an engineering degree from ENSTA Bretagne (Ensieta). He obtained his Ph.D. degree from the University of Orsay - Paris Sud within the L2S-CNRS in 2007. Since 2010, he has been working as a research scientist at the French Aerospace Lab (ONERA). His research interests are focused on nonlinear control theory with application to visual servoing, flexible modes attenuation or maneuver load control. He is a member of the IFAC technical committee on Aerospace.

Erwan Kervendal received an engineering degree in 2005 from ESTACA and a Master of Science in Aerospace Engineering in 2006 from Florida Institute of Technology. Since 2006, he works for Airbus Defence and Space. His present position is Automatic Control, GNC and Formation Flying Group leader in the AOCS/GNC advances studies Department. Main interests of the GNC team are vision-based navigation, GNSS-based navigation, hybridation, as well as Guidance and Control for Space landing, rendezvous and interplanetary journey.

Eric Bornschlegl was working in Avionics and Guidance Navigation and Control systems at ESA/ESTEC.

Franck Ruffier received an engineering degree in 2000 and a PhD degree from INP-Grenoble in 2004 as well as a Habilitation to supervise research (HDR in French) from Aix-Marseille University in 2013. His present position is CNRS Research Scientist and co-Head of the Biorobotics Lab at the Institute of Movement Science (ISM). His main interest areas are vision chips, bio-inspired optic flow processing and biomimetic sensory motor control laws.